

1 **Super Dual Auroral Radar Network Expansion and its**
2 **Influence on the Derived Ionospheric Convection**
3 **Pattern**

4 **M.-T. Walach¹, A. Grocott¹, F. Staples^{2,3}, E. G. Thomas⁴**

5 ¹Lancaster University, Lancaster, LA1 4YW, UK

6 ²formerly at Mullard Space Science Laboratory, University College London, Holmbury St. Mary, RH5
7 6NT, UK

8 ³Department of Earth, Planetary, and Space Sciences, University of California, Los Angeles, CA, USA

9 ⁴Thayer School of Engineering, Dartmouth College, Hanover, NH 03755, USA

10 **Key Points:**

- 11 • We identify changes in derived convection maps when PolarDARN and StormDARN
12 are added, and show the impact of different processing
- 13 • Derived convection parameters are highly susceptible to processing variables and
14 which radars are included
- 15 • We show how the number of backscatter echoes per map is critical to the integrity
16 of the maps, and discuss how this impacts map quality

Corresponding author: M.-T. Walach, m.walach@lancaster.ac.uk

Abstract

The Super Dual Auroral Radar Network (SuperDARN) was built to study ionospheric convection and has in recent years been expanded geographically. Alongside software developments, this has resulted in many different versions of the convection maps dataset being available. Using data from 2012 to 2018, we produce five different versions of the widely used convection maps, using limited backscatter ranges, background models and the exclusion/inclusion of data from specific radar groups such as the StormDARN radars. This enables us to simulate how much information was missing from older SuperDARN research. We study changes in the Heppner-Maynard boundary (HMB), the cross polar cap potential (CPCP), the number of backscatter echoes (n) and the χ^2/n statistic which is a measure of the global agreement between the measured and fitted velocities. We find that the CPCP is reduced when the PolarDARN radars are introduced, but then increases again when the StormDARN radars are added. When the background model is changed from the RG96 model, to the most recent TS18 model, the CPCP tends to decrease for lower values, but tends to increase for higher values. When comparing to geomagnetic indices, we find that there is on average a linear relationship between the HMB and the geomagnetic indices, as well as n , which breaks when the HMB is located at latitudes below $\sim 50^\circ$ due to the low observational density. Whilst n is important in constraining the maps (maps with $n > 400$ data points are unlikely to differ), it is insufficient as the sole measure of quality.

Plain Language Summary

The ionosphere, where space begins and the atmosphere ends, moves as a result of the Earth's magnetic field coupling with the Sun. The Super Dual Auroral Radar Network (SuperDARN) was built around the Earth's magnetic poles to study this phenomenon, known as ionospheric convection. Combining many line-of-sight convection measurements, we are able to build global maps of ionospheric convection from SuperDARN data. This encapsulates dynamics which are central to space weather phenomena. SuperDARN, which has been gathering data for decades, has over time undergone numerous transformations, including the development of new processing software and more radars being added to the network. Using data from the years 2012 to 2018, we perform a statistical analysis on processed SuperDARN convection maps for the entire dataset and assess systematically how the dataset has changed over the years. We consider how the addition of more

49 data and differences to the convection mapping procedures can affect scientific studies
50 in the context of this large database.

51 **1 Introduction**

52 The Super Dual Auroral Radar Network (SuperDARN) consists of high-frequency
53 coherent scatter radars built to study ionospheric convection by means of Doppler-shifted,
54 pulse sequences and has been widely used in space physics and ionospheric research (e.g.
55 Greenwald et al., 1995; Ruohoniemi & Greenwald, 1996; Chisham et al., 2007; Nishitani
56 et al., 2019). SuperDARN data are continuously available from 1993, with the network
57 having expanded over time from one radar (built in 1983) to 23 radars in the Northern
58 hemisphere, 13 in the Southern hemisphere and more under construction (Nishitani et
59 al., 2019). This expansion has allowed for a greater area to be covered by SuperDARN
60 (i.e. down to magnetic latitudes of 40°) with at least 16 different look directions along
61 which each radar can sample different ranges (Nishitani et al., 2019) in the Northern hemi-
62 sphere. Line-of-sight measurements by this large-scale network of radars can be combined
63 and used to construct a picture of high-latitude ionospheric convection on time scales
64 of 1-2 minutes (Ruohoniemi & Baker, 1998). The radars can be grouped into high-latitude
65 radars (the original network), polar-latitude radars (or PolarDARN), and mid-latitude
66 radars (or StormDARN). Nishitani et al. (2019) provides a summary from a historical
67 northern hemisphere perspective: high-latitude radars, at magnetic latitudes of $50\text{-}70^\circ$
68 were first built, starting in 1983 with the Goose Bay radar, followed by the PolarDARN
69 radars (covering $70\text{-}90^\circ$ magnetic latitude), and the expansion to mid-latitudes ($\sim 40\text{-}50^\circ$),
70 starting in 2005 with the Wallops Island radar. Over time new radars have improved global
71 ionospheric convection mapping by increasing the number of measurements and look di-
72 rections.

73 The most commonly used SuperDARN data product by the space science and iono-
74 spheric research community is the convection maps. Convection maps are large scale maps,
75 showing ionospheric convection around the magnetic poles. In order to produce these
76 maps, several data processing steps have to be undertaken. Data from different radars
77 are combined, which allows for the exclusion of data from particular radars or the spec-
78 ification of a range limit for the scatter. For example, slow moving E-region scatter can
79 and should be removed by setting the minimum range gate limit to 800 km (Forsythe
80 & Makarevich, 2017; Thomas & Shepherd, 2018). It has become apparent that far range

81 data beyond 2000 km may also be problematic owing to geolocation uncertainties in the
82 range finding algorithm (Chisham et al., 2008). Once the data has been chosen and com-
83 bined, a fitting algorithm is applied which fits an electrostatic potential in terms of spher-
84 ical harmonic functions to the data (Ruohoniemi & Greenwald, 1996; Ruohoniemi & Baker,
85 1998). To find the optimal solution for the spherical harmonic coefficients, a singular value
86 decomposition (e.g. Press, W. H. and Teukolsky, S. A. and Vetterling W. T. and Flan-
87 nery B. P., 2007) is minimised. When this fitting is performed, typically a background
88 statistical convection model (hereafter referred to as just the background model), param-
89 eterised by a mix of IMF conditions and solar wind velocity depending on the model used,
90 to infill information in the case of data gaps. This method is also known as the ‘Map Po-
91 tential’ technique. With the expansion of the radar network, as well as data processing
92 software improvements, the resulting data product has undergone several changes.

93 Several models are available for the ‘Map Potential’ method, most notably Ruohoniemi
94 and Greenwald (1996) generated the most widely used background model, which was sub-
95 sequently implemented in the RST, the Radar Software Toolkit (e.g. SuperDARN Data
96 Analysis Working Group, Thomas, Ponomarenko, Billett, et al., 2018). This background
97 model was thus used by most SuperDARN users when generating convection maps and
98 used in many scientific studies. Ruohoniemi and Greenwald (1996) used data from the
99 Goose Bay radar to derive the background statistical model. Since then however, many
100 more radars have been added to SuperDARN. This raises the question of how much of
101 an effect changing the background model has on the convection map dataset, which was
102 investigated by Shepherd and Ruohoniemi (2000). The main conclusion from Shepherd
103 and Ruohoniemi (2000) was that the solution becomes insensitive to the choice of sta-
104 tistical model when the data coverage is high. Since then, Ruohoniemi and Greenwald
105 (2005) produced an updated version of their background model using data from 9 radars,
106 but this was not implemented into RST, thus keeping the RG96-model the default which
107 was used by the community. Since then, a number of updated background models, such
108 as Pettigrew et al. (2010), Cousins and Shepherd (2010) and Thomas and Shepherd (2018)
109 have been produced. The Pettigrew et al. (2010) and Cousins and Shepherd (2010) mod-
110 els were not implemented into RST until version 4.1 (SuperDARN Data Analysis Work-
111 ing Group, Thomas, Ponomarenko, Bland, et al., 2018). Soon after, the background model
112 by Thomas and Shepherd (2018) was released, which is now standard in RST since ver-
113 sion 4.2 (SuperDARN Data Analysis Working Group, Thomas, Ponomarenko, Billett,

114 et al., 2018). The RG96 and TS18 models are thus the most widely used and we will fo-
115 cus our analysis on these background models.

116 In this paper we conduct a large scale data analysis to assess systematically how
117 the SuperDARN convection map dataset has changed over the years and how this may
118 have affected the derived convection maps.

119 We specifically probe the effects of the following changes:

- 120 1. Inclusion of the backscatter range limits
- 121 2. Addition of the PolarDARN data
- 122 3. Addition of the StormDARN data
- 123 4. Updating of the background statistical model

124 Comparing different versions of input dataset allows for a large-scale analysis of
125 systematic changes and in particular, how the introduction of new StormDARN and Po-
126 larDARN data modifies the convection maps on a large scale, which has implications for
127 use of the maps in scientific studies.

128 In particular, we discuss measures of map quality in the context of these changes,
129 as well as the placement of the Heppner-Maynard boundary (the lower latitude convec-
130 tive boundary which is used to constrain the maps).

131 **2 Data and Method**

132 To provide a meaningful large scale comparison of different versions of the Super-
133 DARN dataset, we process Northern hemisphere data to create different versions of the
134 SuperDARN convection maps for the same time period (2012-2018).

135 To make SuperDARN convection maps we process the raw data using the Radar
136 Software Toolkit (RST (SuperDARN Data Analysis Working Group, Thomas, Ponomarenko,
137 Bland, et al., 2018)), which can be broken down into 5 steps:

- 138 1. Fitacf files, which include the line-of-sight velocity data, are produced from the
139 raw radar data by applying version 2.5 of the FITACF function (SuperDARN Data
140 Analysis Working Group et al., 2019).
- 141 2. The data from one hemisphere (in our case, the Northern hemisphere) are then
142 gridded onto an equal area latitude-longitude grid (see equation 1 from Ruohoniemi

143 & Baker, 1998) and split into typically one or two minute cadence records. The
 144 grid we use for this analysis is in the AACGM coordinate system (version 2 by Shep-
 145 herd, 2014). Historically it has almost always been the case that all ionospheric
 146 data measured by the radars were added to the grids. As discussed below, we ex-
 147 plore changing the range limit by setting the minimum range gate limit to 800 km
 148 and the far range data limit to 2000 km.

149 3. A Heppner-Maynard boundary (HMB) (Heppner & Maynard, 1987), the low-latitude
 150 boundary of the convection pattern where the flows approach zero, can either be
 151 specified or be chosen using backscatter measurements. This is to constrain the
 152 convection pattern when the spherical harmonic fit is applied (Shepherd & Ruo-
 153 honiemi, 2000). For typical two minute cadence convection maps, it is appropri-
 154 ate to find the lowest latitude where three radar velocity measurements are greater
 155 than 100 ms^{-1} to define the HMB (Imber et al., 2013). This boundary is circu-
 156 lar around the nightside and oval-shaped on the dayside, such that it moves to higher
 157 latitudes. Previous to Shepherd and Ruohoniemi (2000), a fully circular bound-
 158 ary was used, which was deemed to create unrealistic flows at lower latitudes when
 159 the radar network was expanded. To make all the convection maps (D0 to D4),
 160 using RST, the HMB (Heppner & Maynard, 1987; Shepherd & Ruohoniemi, 2000)
 161 was chosen using the default method using the functional form Shepherd and Ruo-
 162 honiemi (2000), using the thresholds above.

163 4. A background model is selected based on solar wind conditions and model vec-
 164 tors are added to the grid. For this, we use solar wind data from the ACE space-
 165 craft, which has been time-lagged to the magnetosphere using the algorithm from
 166 Khan and Cowley (1999) which takes magnetosheath transit time into account.
 167 We add the model, specifying a fitting order of 6 with a ‘light’ doping level for the
 168 background convection model, which means a minimum reliance is placed on the
 169 background model. Newer background models (Thomas & Shepherd, 2018; Pet-
 170 tigre et al., 2010; Cousins & Shepherd, 2010) are all generated using a fitting or-
 171 der of 8, whereas Ruohoniemi and Greenwald (1996) was generated using a sixth
 172 order fit.

173 5. Finally, the ‘Map Potential’ technique is applied. We use the technique from Ruohoniemi
 174 and Baker (1998) to fit electrostatic potentials to the combined measured and model
 175 velocity vectors as spherical harmonic functions.

176 Using the steps outlined above, we first create the dataset (D0) with the high-latitude
177 radars only, which is then modified by changing one aspect for each subsequent dataset.
178 This allows us to contrast the impact of each change in the dataset. The basic data pro-
179 cessing is the same for all the datasets, except for the differences outlined in Table 1. The
180 specific processing commands and options used for the data processing can be found in
181 the appendix of this paper.

182 Two versions of the gridded map files were created (e.g. step 2 to 5 is repeated)
183 to see how changing the backscatter range limits affects the dataset. One version of the
184 gridded files was created with added backscatter range limits and one without any range
185 limit. By only including data from a minimum range of 800 km and a maximum far range
186 of 2000 km, we try to eliminate all possible E-Region scatter and all backscatter with
187 higher uncertainties in range and azimuth (i.e. projected location) (Chisham et al., 2008;
188 Forsythe & Makarevich, 2017; Thomas & Shepherd, 2018). On a statistical level, we ex-
189 pect this method to remove most of the data with higher uncertainty, but this method
190 will also remove some good quality data as a substantial amount of scatter comes from
191 ranges greater than 2000 km. Applying these range limits may not remove all E-region
192 scatter or all scatter with uncertain locations, but currently no better method for a large
193 statistical dataset exists. The version of gridded files with backscatter range limits is used
194 for D1-D4 and the one without a range limit is used for D0. The gridded map files were
195 resolved into two minute records and used the Chisham virtual height model (Chisham
196 et al., 2008).

197 Dataset versions D0 and D1 include the same radars, whereas for D2 and D3, more
198 radars were included (see Table 1). For the selection of PolarDARN and StormDARN
199 groupings the list provided by Table 1 in Thomas and Shepherd (2018) was used. The
200 list provided in Thomas and Shepherd (2018) demonstrates that most of the StormDARN
201 radars were built after the high-latitude and PolarDARN radars.

202 For D4, we keep the selection of radars the same as D3, but use the background
203 model from Thomas and Shepherd (2018) (TS18) instead of the one from Ruohoniemi
204 and Greenwald (1996) (RG96).

205 Having established this archive of 2-minute resolution convection map files, we then
206 extract a set of measured parameters with which to quantify the ionospheric convection.
207 The HMB latitude and cross polar cap potential (CPCP) describe the spatial extent and

208 strength of the convection and allow us to examine how changes in the processing might
 209 affect conclusions of scientific studies, whereas the number of backscatter echoes per map
 210 or the average number of backscatter points per radar allows us to study how changes
 211 affect coverage. In this study, we define the HMB latitude as the latitude of the fitted
 212 boundary on the nightside and we also investigate how this parameter changes along-
 213 side the minimum latitude where backscatter is obtained (Λ_{min}), which can be along any
 214 magnetic local time or longitude. We would thus expect the difference between the two
 215 parameters to be positive for well constrained maps (i.e. Λ_{min} is at a lower latitude than
 216 the HMB), but to be negative when either the minimum latitude of observations is on
 217 the dayside (where the HMB shifts to higher latitudes) or an indicator that the HMB
 218 is not constrained by data. We also show how the different processing affects the χ^2/n -
 219 statistic, which is often used as a global measure of map quality.

220 The χ^2 parameter is a result from the singular value decomposition, which is min-
 221 imised when the spherical harmonic fitting is performed to find the optimal solution for
 222 the coefficients. Ruohoniemi and Baker (1998) define this as

$$223 \quad \chi^2 = \sum_{i=1}^N \frac{1}{\sigma_i^2} [\mathbf{V}[i] \cdot \hat{\mathbf{k}}[i] - W_i]^2, \quad (1)$$

224 where $\mathbf{V}[i]$ is the fitted velocity vector at the grid cell position i , σ_i^2 is standard devi-
 225 ation of the fitted velocity vector at i , $\hat{\mathbf{k}}[i]$ is the direction of the velocity vector, W_i are
 226 the uncertainties associated line-of-sight velocity uncertainties and the dot product thus
 227 provides the projection of the velocity onto the line-of-sight direction. χ^2/n was intro-
 228 duced by Ruohoniemi and Baker (1998) as a measure of the goodness of fit of the spher-
 229 ical harmonic expansion to the measured line-of-sight velocity data, where a value of 1
 230 would indicate a good match and higher values would indicate a worse match. In this
 231 study we explore how this parameter varies and we discuss if it is an adequate measure
 232 of map quality. We discuss why χ^2/n might change and what these changes might mean
 233 for the quality of the convection maps.

234 Additionally, we also discuss the relationship between the HMB latitude and mea-
 235 sures of geomagnetic activity, such as the Auroral Lower index (AL), the Auroral Elec-
 236 trojet index (AE) and the Symmetric Horizontal index (Sym-H) (Davis & Sugiura, 1966;
 237 Iyemori, 1990). These are derived from ground-based magnetometer measurements and
 238 are a proxy for the magnetospheric activity in response to the dayside driving and in-

239 ternal dynamics (Davis & Sugiura, 1966; World Data Center for Geomagnetism in Ky-
 240 oto et al., 2015). We also consider the relationship between the CPCP and Φ_D , the day-
 241 side reconnection rate, which is calculated from the IMF B_{YZ} component, the solar wind
 242 speed, V_X , and IMF clock angle, θ , (Milan et al., 2012; Walach et al., 2017):

$$243 \quad \Phi_D = 3.3 \times 10^5 V_x^{4/3} B_{YZ} \sin^{9/2} \frac{1}{2} \theta \quad (2)$$

244 We compare these parameters from D0 to D3 with D4, the most modern set-up,
 245 which we use as our control dataset. We compare D0 and D4 to see how the lack of a
 246 range limit, PolarDARN, StormDARN and an updated background model affects the
 247 convection maps. We compare D1 to D4 to see how the lack of PolarDARN, StormDARN
 248 and an updated background model affects the convection maps, and a D2 to D4 com-
 249 parison allows us to investigate the lack of StormDARN and an updated background model
 250 affects the convection maps. Finally, a comparison between D3 to D4 allows us to see
 251 the effects on the convection maps of changing the background model only. Overall, this
 252 allows us to see which changes take us closer to the control dataset, D4. The timeseries
 253 data extracted from the SuperDARN convection maps is condensed into probability dis-
 254 tribution functions (PDF) for each parameter. Our approach allows us to further inves-
 255 tigate how changing one parameter affects the convection maps (e.g. comparing the PDF
 256 of D1 and D4 to the PDF of D0 and D4 of the same parameter shows how adding range
 257 limits affects the dataset). In section 3.5 we also explore by how much the fitted Super-
 258 DARN velocities can increase after adding StormDARN. In the following section, we show
 259 the PDFs, which enable us to compare the effects of changing the dataset on each pa-
 260 rameter in turn. A selection of example convection maps, that illustrates some of the dif-
 261 ferences that result from changing the datasets, are shown in the Supporting Informa-
 262 tion (Figure S1).

263 **3 Results**

264 This section shows the probability distribution functions for the parameters dis-
 265 cussed above. We compare the results from each dataset with the control dataset (D4)
 266 and discuss the parameters in turn.

Table 1. Differences between the comparison datasets

Version	Introduced difference	Background model	high-latitude radars	range limits	PolarDARN radars	StormDARN radars
D0	High-latitude radars ^a only	RG96	yes	no	no	no
D1	Added range limits: 800-2000 km	RG96	yes	yes	no	no
D2	Added PolarDARN radars ^b	RG96	yes	yes	yes	no
D3	Added all other (i.e. StormDARN radars) ^c	RG96	yes	yes	yes	yes
D4: Con- trol set	Changed the back- ground model	TS18	yes	yes	yes	yes

^a High-latitude radars: King Salmon, Kodiak, Prince George, Saskatoon, Kapuskasing, Goose Bay, Stokkseyri, Pykkvibaer, Hankasalmi.

^bPolarDARN radars include: Inuvik, Rankin Inlet, Clyde River, Longyearbyen.

^cStormDARN radars include: Hokkaido West, Hokkaido East, Adak West, Adak East, Christmas Valley West, Christmas Valley East, Fort Hays West, Fort Hays East, Blackstone, Wallops Island.

267

3.1 The Heppner-Maynard Boundary

268

269

270

271

Figure 1 shows the probability distribution functions comparing the HMB latitude between models with the difference between the HMB latitude and Λ_{min} . The occurrences of the example maps in Fig. S1 are indicated in the probability distribution functions by the light blue crosses (and green square for comparison of Fig. S1 g and h).

272

273

274

275

276

277

278

279

280

281

282

283

284

285

286

287

288

289

290

291

292

293

294

295

296

297

Fig. 1a shows the comparison between D0 and D4. Whilst for a large proportion of the data (38%) the HMB does not differ ($\pm 1^\circ$), 44% of the data lie above the line of unity. For these instances the HMB is placed at a higher latitude in D4 than in D0. This is mostly prominent when the HMB for D0 is above latitudes of 59° (40% of the time). This could be due to a number of reasons, which we will discuss in section 4. We also see a saturation of points in D0 at a HMB latitude of 60° , which is where the boundary is drawn if not enough data is available (due to low data coverage or no slow scatter being observed). The RG96 model has two boundaries where the HMB can be drawn when not enough data is available: 60° and 55° , whereas TS18 interpolates between background model solutions, so there are less discrete groupings in the HMB locations. Fig. 1b shows the HMB latitude comparison between D1 and D4. Adding range limits brings the HMB distribution closer to the D4 dataset, but the saturation at 60° remains, which means the HMB is most likely relying on the background fitting. This could be due to a lack of StormDARN data. Now including the PolarDARN data, Fig. 1c shows the D2 dataset once more moving closer to the D4 dataset: The HMB moves to higher latitudes in D2 for 27% of the time. The HMB moves to higher latitudes in D2 if it cannot be defined by data in D1. For the majority of maps however (72%), the HMB does not differ at all when adding PolarDARN data. For D3 and D4, the HMB values are largely the same as the raw input data do not differ, except for times when the HMB cannot be defined. For brevity, we have chosen not to show this plot, as these cases are extremely rare (3% of cases). For D4, these cases will be defined by the background model and vary smoothly due to the interpolation in the background model between distinct bins, whereas for D3 (due to the parametrization in RG96), they will be defined as two distinct latitudes, as defined by the model: 60° (96% of instances) and 55° (4% of instances), where the 60° is the default and 55° is defined for strong, southward IMF ($6 \text{ nT} < |B| < 12 \text{ nT}$; $90^\circ < \text{clock angle} < 270^\circ$).

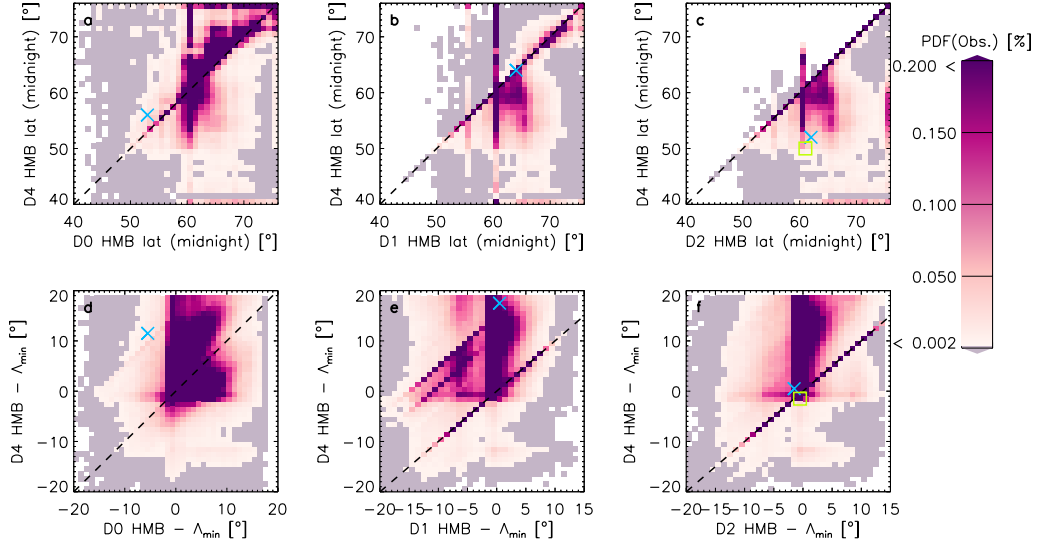


Figure 1. Probability distribution functions comparing the HMB latitude for (a) D0; (b) D1; (c) D2 with D4; and the difference between the HMB latitude and Λ_{min} for (d) D0; (e) D1; (f) D2 with D4. The occurrences of the example maps in Fig. 1 are indicated in the PDFs by blue crosses and green square.

298 Fig. 1d shows the difference between the HMB latitude and Λ_{min} for D0 against
 299 D4. This difference is mostly positive for both D0 and D4, which means that the HMB
 300 sits poleward of Λ_{min} and is thus well constrained. Fig. 1e shows the same parameter,
 301 but comparing D1 and D4. Having added range limits, more data is in the top left quad-
 302 rant of the plot than previously, where D1 is negative and D4 is positive. For these data,
 303 introducing range limits means the HMB is not well-defined in D1, but it is remedied
 304 in D4. Fig. 1f shows the same parameter, but comparing D2 and D4. Adding the Po-
 305 larDARN data moves a considerable proportion of these data with negative HMB- Λ_{min}
 306 and more datapoints cluster around 0, meaning that for these maps, the fitting is likely
 307 to be better constrained. It is worth noting however that even when this parameter is
 308 at 0, the HMB is not necessarily bounded due to no observations being available equa-
 309 torward.

310

3.2 Number of Backscatter echoes

311

312

Figure 2 shows probability distribution functions for n , the number of backscatter echoes and the average n per radar.

313

314

315

316

317

318

Fig. 2a shows n for D0 versus D4. Going from D0 to D4, the number of backscatter points largely increase (67% of the time), though sometimes n decreases (32% of the time), which means the introduction of range limits reduces n by more than the combined addition of Polar and StormDARN increase it by. Introducing range limits (see Fig. 2b), means that for all instances, n is either higher or the same in D4 as in D1 and the same is true for D2, after the PolarDARN data have been added (see Fig. 2c).

319

320

321

322

323

324

325

326

Fig. 2d shows that the number of backscatter points per radar is on average higher for D0 than D4. After introducing range limits, however (Fig. 2e), this is true for a slightly smaller proportion of the data. After adding the PolarDARN data (Fig. 2f), we see that despite a large proportion of the data still lying below the line of unity, the gradient of the relationship has increased which means that the number of backscatter echoes per radar is higher for the StormDARN than the PolarDARN. By comparing Fig. 2d to e and f, we find that number of backscatter echoes per radar is lower for PolarDARN than the older radars in the network (D0 and D1).

327

3.3 CPCP and χ^2/n

328

329

330

331

332

333

334

335

336

337

338

339

340

Figure 3 shows a comparison between the different datasets and D4 for the CPCP (a to d) and χ^2/n (e to h). We immediately see that the CPCP varies little on average. Fig. 3a shows that the observed CPCP is on average smaller for D4 than D0 (54% of the time), but can increase or decrease from D0 to D4. When the CPCP increases (going from D0 to D4), it increases by more on average (8 kV median increase; 10 mean increase; 92 kV maximum increase; 8 kV standard deviation of the increase) than the average decrease (7 kV median decrease; 8 kV mean decrease; 98 kV maximum decrease; 5 kV standard deviation of the decrease). The increases happen however less frequently than the decreases (46% of the time, compared to the 54% of the time). We see vertical striations in the data in Fig. 3a, which is due to the CPCP being discretely quantized by the RG96 model bins when the model influence is strong, whereas for TS18 interpolation between model bins occurs. Fig. 3b shows the CPCP distribution for D4 and D1. Not much varies after introducing range limits, but we find that the striations are more pronounced. Com-

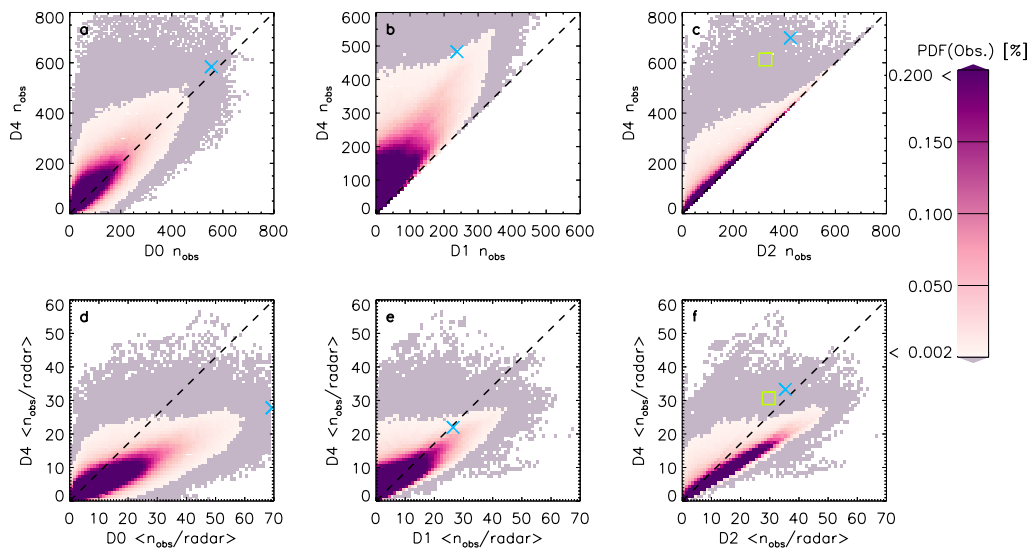


Figure 2. Probability distribution functions comparing the number of backscatter echoes for (a) D0; (b) D1; (c) D2 with D4; and the average backscatter echoes per radar for (d) D0; (e) D1; (f) D2 with D4. The occurrences of the example maps in Fig. S1 are indicated in the PDFs by blue crosses and green square.

341 paring D1 and D4 and looking at the vertical spread, it is possible for the CPCP to in-
 342 crease by more than 30 kV, though the majority of data lies below the unity line and
 343 is likely to decrease by less than ~ 30 kV. Adding in the PolarDARN data (Fig. 3c) moves
 344 the D2 CPCP closer to the D4 CPCP, but there is still some spread. We see less of the
 345 vertical striations in the CPCP for D2 than previously, which means the background model
 346 has reduced influence. Fig. 3d shows the CPCP comparison between D3 and D4. After
 347 adding StormDARN data, there is little variation in the distribution in comparison to
 348 Fig. 3c. At the lower range (0- ~ 50 kV), the CPCP is likely to decrease as we change the
 349 background model from RG96 to TS18 (this occurs 42% of the time as opposed to the
 350 increase which occurs 29% of the time). For the higher range (>50 kV) however, the CPCP
 351 is likely to increase when we change model from RG96 (D3) to TS18 (D4) (this occurs
 352 16% of the time as opposed to the decrease which is 13%). Overall, TS18 thus provides
 353 a lower CPCP 55% of the time and a higher CPCP 45% of the time for the same data.
 354 The majority of data lies below the unity line and is likely to decrease by less than ~ 30
 355 kV.

356 Fig. 3e shows χ^2/n for D0 and D4. Most of the distribution lies between 1 and 10
 357 for both datasets. We find that for the times when χ^2/n is larger in D4 than D0, n for
 358 D4 tends to small numbers (<200 ; 102 median; 123.13 mean). Fig. 3f shows the same
 359 distribution, but for D1 and D4. Changing the data from D0 to D1, the split between
 360 increases and decreases is approximately equal (45% of χ^2/n increasing and 50% of χ^2/n
 361 decreasing). Adding the PolarDARN data (Fig. 3g), shows a slightly slimmer distribu-
 362 tion in the y-direction, meaning that the parameter in D2 has moved closer to D4. The
 363 distribution moves yet closer to D4, after we add the StormDARN data (Fig. 3h). Al-
 364 though not immediately obvious, 64% of the data lie below the line of unity (in compar-
 365 ison to 36% of data above the line) in Fig. 3h, meaning the fitting error is on average
 366 reduced when making the convection maps using TS18 in comparison to RG96.

367 **3.4 Differences in Velocity after Adding StormDARN**

368 Computing the velocities for D3 at the HMB latitude location in D2 can be used
 369 as an indicator of how much the map has changed at specific locations and gives us an
 370 idea of how quantitatively different the convection maps might be without the Storm-
 371 DARN radars. Choosing the HMB allows us to see the maximum expected variation.
 372 We explore this in more detail now.

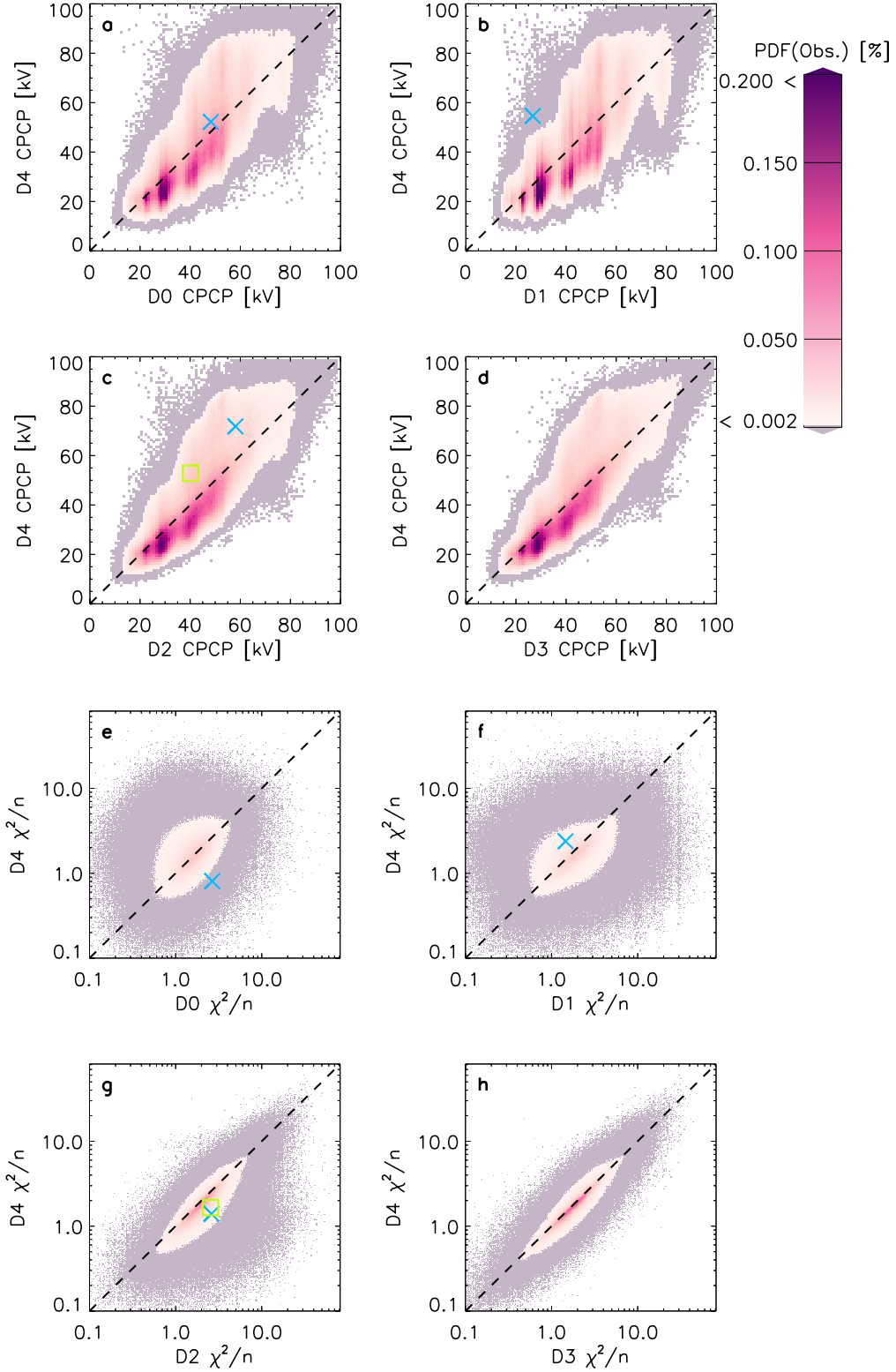


Figure 3. Probability distribution functions comparing the CPCP for (a) D0; (b) D1; (c) D2 ;(d) D3 with D4; and the χ^2/n distribution for (e) D0; (f) D1; (g) D2 ;(h) D3 with D4. The occurrences of the example maps in Fig. S1 are indicated in the PDFs by blue crosses and green square.

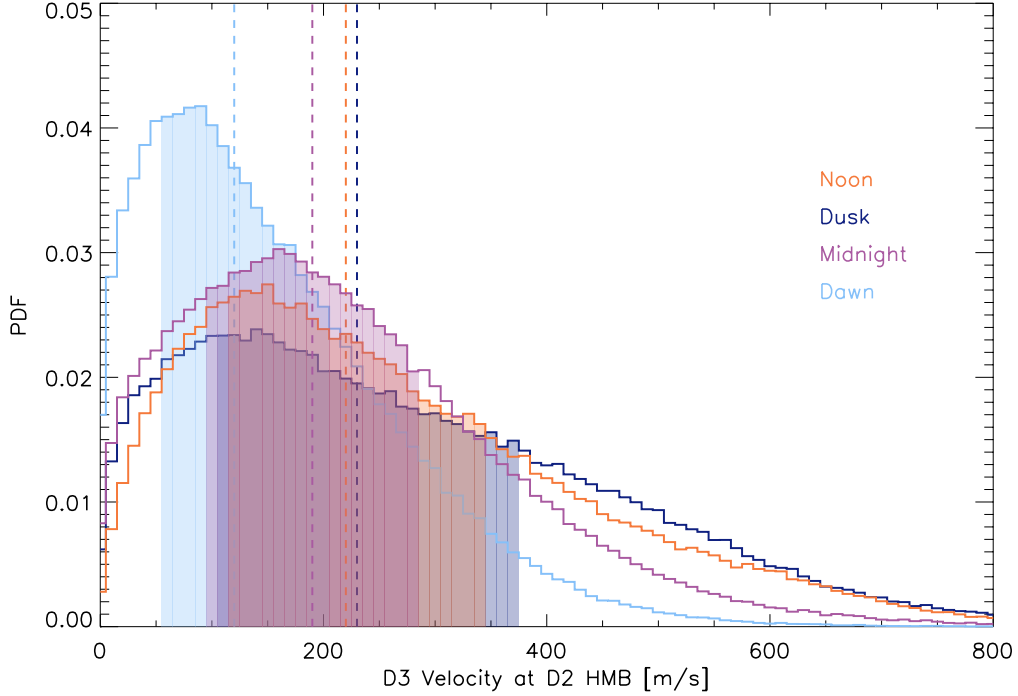


Figure 4. Probability distribution function of the velocity for D3, extracted at the noon, dusk, midnight and dawn locations where D2 would have had the HMB. Dashed lines show the medians for each distribution. Shaded regions indicate the boundaries of the lower and upper quartiles (25% and 75%).

373 Figure 4 shows the velocities, extracted from the D3 convection maps for the lo-
 374 cations where the D2-HMB intersects with the noon, dusk, midnight and dawn meri-
 375 dians. After adding the StormDARN data, the maps differ considerably at the locations
 376 where the HMB would have otherwise stipulated that there be zero flow. The histograms
 377 show that at dawn, the effect is the least noticeable and that there is a 1 in 2 chance that
 378 the velocity measured in D3 has increased by 120 m/s or less, whereas this increases to
 379 190 m/s for midnight and 220 m/s and 230 m/s for noon and dusk, respectively. In 8%
 380 of cases (which equates to over 22000 maps), adding StormDARN increases the D2-zero
 381 flow regions at midnight to > 400 m/s at midnight, which indicates a considerable dif-
 382 ference to the convection pattern.

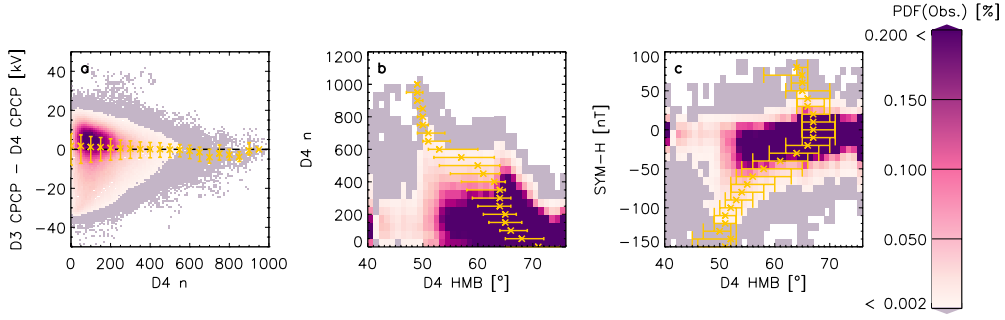


Figure 5. Probability distribution functions comparing D3 and D4 datasets: (a) CPCP difference versus n , (b) n versus D4 HMB, (c) Sym-H versus D4 HMB. The black dashed line show the line at 0 and the yellow crosses show the median for the associated bins and the error bars represent the upper and lower quartiles of the distributions (75% and 25%).

383

3.5 Number of Backscatter Points in Context

384

We have already shown most of the differences which happen to the derived convection maps when changing the background model. Figure 5 shows further data on how changing n in D3 and D4 relates to parameters of interest (e.g. CPCP variation, HMB and Sym-H).

385
386
387

388

Figure 5a shows the CPCP difference against n . We find that the CPCP shows the least variability for maps with a high number of backscatter points, which means that there is a model dependency which decreases as n increases. For example, at $n=200$, the median and standard deviation are 0.87 kV and 8.88 kV, whereas at $n=400$, the median and standard deviation are 0.04 kV and 6.50 kV, respectively. The yellow crosses and error bars (which are indicative of the median and upper or lower quartiles) illustrate further that the distribution is narrowing as n increases. While using the TS18 model tends to result in a lower CPCP for less constrained maps, it can also overall result in a significantly larger CPCP than with RG96 Fig. 5b shows the D4 HMB latitude against n . It shows that the HMB is likely to move closer to the equator as the number of backscatter echoes increases. This is again illustrated by the yellow crosses and error bars. Fig. 5c shows the HMB latitude against Sym-H. There is a dependence in the HMB moving to lower latitudes as Sym-H becomes more negative. Panels b and c show a seemingly linear trend with HMB, which seems to break at low latitudes, but this is not supported by the yellow crosses, which show the medians for each bin.

389
390
391
392
393
394
395
396
397
398
399
400
401
402

403 3.6 Changes to Convection Mapping Since the Original Auroral Radars

404 Since the SuperDARN radar network was first built, new additions to the network
 405 have resulted in differences to the convection map dataset. In this section we compare
 406 D0 and D4 further to see this historical comparison in context. Figure 6 shows further
 407 distributions comparing D0 and D4 in the context of geomagnetic activity. Fig. 6a shows
 408 the differences in the CPCP between D4 and D0 against the dayside reconnection rate,
 409 Φ_D . The differences in the CPCP tend to be smaller for high solar wind driving (high
 410 Φ_D). Similarly, Fig. 6b shows the differences in the HMB against AE and Fig. 6c shows
 411 the estimates in the HMB against AL. Panels b and c show that differences in the HMB
 412 tend to be smaller when the auroral electrojet indices, AE and AL are enhanced. Figs.
 413 6d and e show the D0 and D4 HMB against AL. These include yellow and blue crosses
 414 which represent the median fits for each AL bin with the error bars showing the lower
 415 (25%) and upper (75%) quartiles of the distributions, allowing us to compare D4 (yel-
 416 low) with D0 (blue). This shows very clearly that when we use D0, we are less likely to
 417 observe a low HMB at enhanced (low) AL, which is not to mean that these occurrences
 418 do not exist, but simply that the SuperDARN fitting with the original dataset means
 419 we are less likely to observe them. In Figs. 6f and g, we provide a similar comparison for
 420 the D4 and D0 CPCP with respect to Φ_D . Here, we use the vertical bins to calculate
 421 the upper and lower quartiles and the medians. We show error bars for every fifth bin
 422 only due to the point density. This comparison shows that for D4 we are more likely to
 423 observe a higher CPCP at higher values of Φ_D than for D0. In fact, at a Φ_D of 100 kV,
 424 the median CPCP for D4 is at ~ 75 kV and ~ 65 kV for D0. The median curve has a
 425 different shape for the two datasets: The bulk of the distribution is at low values of so-
 426 lar wind driving where the median values are very similar but at higher values, the dis-
 427 tributions differ. Both have a logarithmic shape to them and neither appear like a lin-
 428 ear fit would suffice to describe the trend in the dataset. Finally in panel h, we show the
 429 ratio between the CPCP normalised by Φ_D for both datasets. This shows that the ra-
 430 tio between the two versions of the CPCP and dayside driving are proportional to each
 431 other. It also shows that these ratios increase logarithmically and that the CPCP dif-
 432 ferences with respect to Φ_D in D0 are likely to be similar to D4.

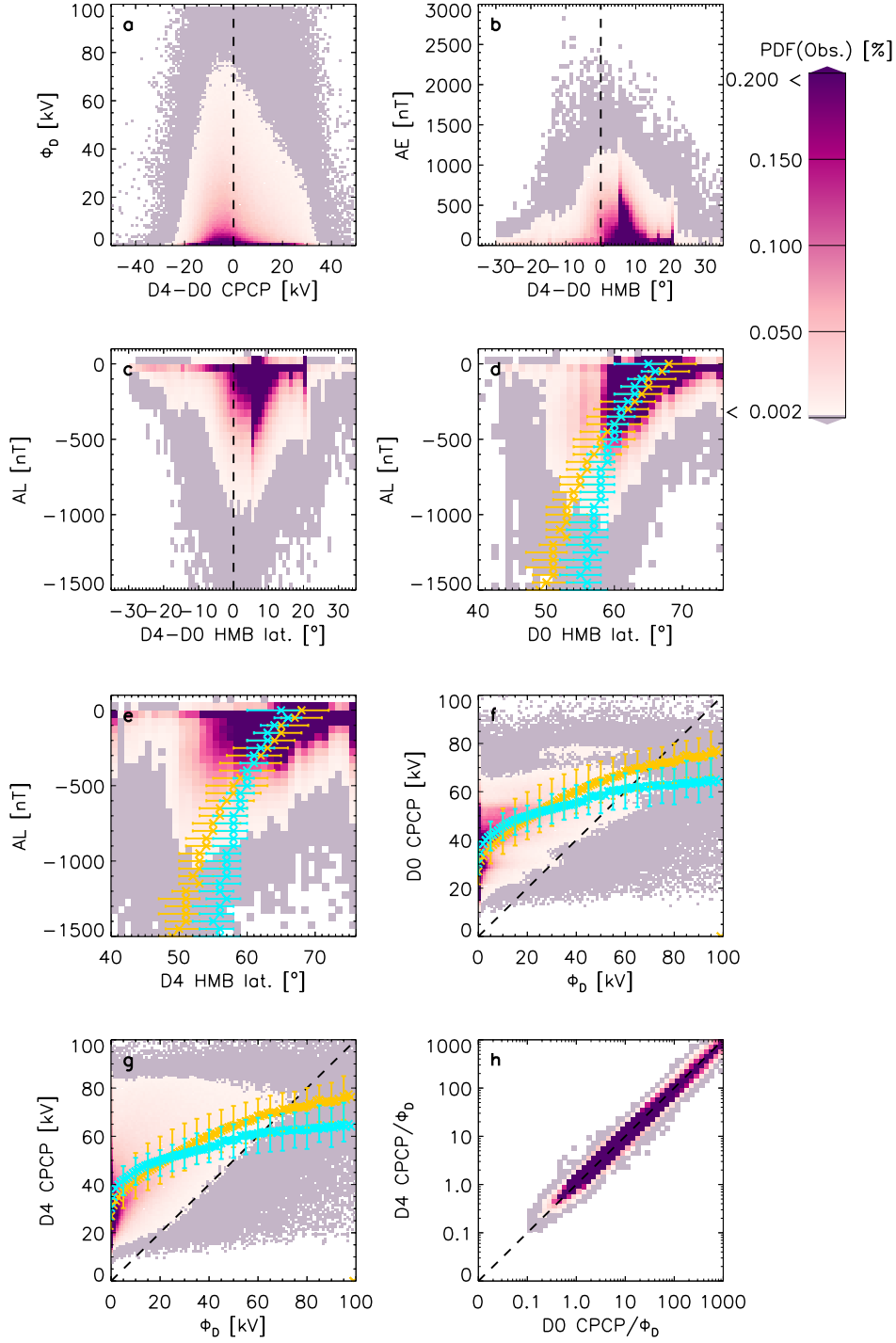


Figure 6. Probability distribution functions comparing the entire D0 and D4 datasets: (a) Φ_D versus the CPCP difference, (b) AE versus HMB difference, (c) AL versus HMB difference, (d) AL versus D0 HMB and (e) D4 HMB, (f) D0 CPCP versus Φ_D , (g) D4 CPCP versus Φ_D and (h) CPCP normalised by Φ_D . The crosses show the median in the x- or y-direction for each y- or x-bin (where applicable) with the yellow showing the fit for D4 and blue showing the fit for D0. Error bars represent the lower and upper quartiles of the distributions (25% and 75%, respectively). Black dashed lines either show the lines of unity or the line at 0.

3.7 Identification of Minimum Map Reliability

When using SuperDARN maps in research, a frequent question is “How reliable is this map?” and often n is used to answer this question. If n is high, the maps are often deemed more reliable, but is there a universal limit for n , which can be used to select reliable convection maps?

To attempt to answer this question statistically, we present in Figure 7a the PDF of the ratio of χ^2/n between D4 and D0 on a logarithmic scale against the difference in n . It shows that as the map fitting becomes more constrained (i.e. the ratio of D4 and D0 χ^2/n comes closer to 1), the difference in n is likely to become smaller. As the ratio of χ^2/n becomes larger, the difference in n is also very small. This means that an increase in n does not necessarily translate to an improved map. In fact, the width of the distribution peaks in the y-direction (and differences in n are more likely to happen) for maps that are not already well constrained. Fig. 7a shows that maps where χ^2/n does not differ much (i.e. ratio close to 1), the differences in n are also very small, but can also be large. Figure 7b and c show the ratio of the two χ^2/n on a logarithmic scale versus n in D4 and n in D0. There is a trend for χ^2/n ratio moving away from 1 as n decrease. In both D4 and D0, there is no clear uniform break-point in n , where χ^2/n ratio becomes smaller and the maps are better constrained in D4 than D0. We also find that as n increases, χ^2/n is likely to be smaller for D4 than D0, however there is less spread and the peak is more pronounced for D0 than D4. We also note that the tail in the distributions of D4 n and D0 n versus the ratio in χ^2/n are not symmetrical around 0. We will discuss these results further in the discussion section.

4 Discussion

4.1 Effect of Changing Range Limits on Derived Convection Maps

Adding range limits is intended to remove E-region scatter (i.e. scatter which moves slower than F-Region scatter), which can be assessed by direct comparison between D0-D4 and D1-D4. If we consider a simple situation where adding a range limit removes scatter moving slower than the F-region ExB velocity, then this should increase overall convection in the maps and thus the CPCP should increase. However, the blanket removal approach means that the removed scatter can also be faster than the average F-region flows, which can lead to counter-intuitive results. This will be discussed in further de-

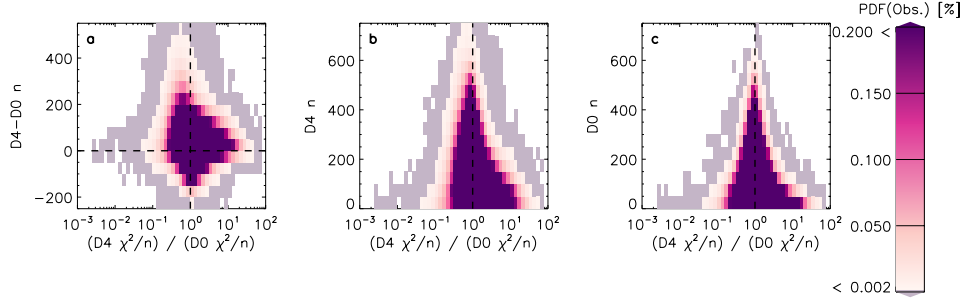


Figure 7. Probability distribution functions comparing the D0 and D4 datasets: The ratios of χ^2/n on a logarithmic scale versus (a) the differences in n , (b) D4 n and (c) D0 n . The black dashed line show the line at 0 (horizontal lines) or 1 (vertical lines).

464 tail later in this section. The applied range limits also remove far-range scatter from slant
 465 range > 2000 km, which avoids potential errors in geolocation of LOS measurements at
 466 far range gates. Whilst this seems like it should constrain the spherical harmonic solu-
 467 tion, Thomas and Shepherd (2018) have shown that the opposite is true for a dataset
 468 that is limited in latitudinal coverage: Figure 11 in Thomas and Shepherd (2018) shows
 469 how range limits impacts the data coverage afforded by the high-, polar-, and mid-latitude
 470 radars. For example, when data from beyond 2000 km slant range are removed from the
 471 high-latitude radar dataset, which is comparable to our D0 to D1 variation, then the so-
 472 lution poleward of $\sim 76^\circ$ magnetic latitude is purely reliant on the statistical model be-
 473 cause no measurements are possible. This is to be expected and will be the same for our
 474 D0 to D1 comparison. Imposing the range-limit will also reduce the number of backscat-
 475 ter echoes in the maps but we also see that the number of backscatter echoes are not solely
 476 responsible for map quality.

477 Chisham and Pinnock (2002) conclude that the contamination from non-F-region
 478 scatter does not usually have a large impact on the global characteristics of the Super-
 479 DARN convection maps. However, they did show that it has a significant effect on mesoscale
 480 features in the convection maps. Our study supports these findings in terms of the larger
 481 scale characteristics. We find that for the analysed time period, the CPCP is $> 10\%$ dif-
 482 ferent 5% of the time and the CPCP is $< 10\%$ different 95% of the time. Whilst less than
 483 5% seems like a small set of observations, this does comprise more than 80000 maps, so
 484 it may be important on a case-study basis.

485 Chisham and Pinnock (2002) further showed that removing E-region scatter may
 486 not always result in more accurate convection maps. Whilst most E-region scatter is be-
 487 lieved to move slower than F-region scatter, this may not always be the case: Forsythe
 488 and Makarevich (2017) used SuperDARN data from the Southern hemisphere and showed
 489 that E-Region scatter can be of a similar order of magnitude as F-Region scatter (~ 200
 490 m/s or larger). They also showed however that whilst F-Region scatter tends to have
 491 a Gaussian velocity profile, the E-Region velocity distribution is highly asymmetric, ow-
 492 ing to the Farley-Buneman and gradient drift instabilities being the main drivers. This
 493 may be the reason why Chisham and Pinnock (2002) find that removing E-region scat-
 494 ter does not always improve convection maps, but the study by Forsythe and Makare-
 495 vich (2017) provides clear evidence why removing this scatter makes scientific sense. Our
 496 method of adding range limits follows the strategy of Thomas and Shepherd (2018), though
 497 they used this method for statistical convection maps and this may not always be prac-
 498 tical for instantaneous convection maps. Whilst the method employed here to remove
 499 far range backscatter is a broad-brush approach and also removes valid data, future al-
 500 ternatives could include the use of either calibrated elevation angles (which involves mea-
 501 suring the elevation angles using interferometry) or a more accurate virtual height model.

502 We have to consider the possibility that removing the far-range scatter reduces the
 503 integrity of the maps: The uncertainty in the geolocation of far-range scatter is expected
 504 to be of the order of ~ 100 to 200 km when using the Chisham virtual height model, which
 505 approximately equates to between one to two grid cells. Given that for an order 6 SHA
 506 fit the spatial resolution of the maps is relatively low, this level of spatial uncertainty is
 507 small.

508 To reduce measurement uncertainty, we remove both potential E-region scatter and
 509 scatter from far range gates. We find that by introducing range limits, the normalised
 510 Chi-squared distribution of the map fitting procedure, χ^2/n is increased 74% of the time
 511 and decreased 26% of the time.

512 Sometimes, reducing the number of backscatter points by introducing range lim-
 513 its will increase the HMB to higher latitudes due to removing lower-latitude scatter but
 514 more importantly, this difference will reduce E-region scatter at lower-latitudes and thus
 515 reduce the probability of choosing a HMB at a low latitude. For the subset of observa-
 516 tions where this is most likely the case (i.e. the difference between the HMB and Λ_{min}

517 are greater in D0 than in D1 and the HMB is at a lower latitude in D0 than in D1), the
 518 median n is higher (D0: 128 and D1: 56) than the median for the entire dataset (D0:
 519 93 and D1: 40). Other portions of the dataset which may indicate a worse fitting con-
 520 tain the population where χ^2/n increases: here, the median n is less (D0: 86 and D1:
 521 38) than the medians for the entire dataset (D0: 93 and D1: 40). Both these statistics
 522 suggest, that n is not a good predictor for how good the fit is once range limits have been
 523 introduced if χ^2/n is used as a quality-of-fit indicator. Alternatively, we suggest that this
 524 illustrates a problem with χ^2/n and that it may not be the perfect indicator for qual-
 525 ity. We propose that in the future, a better measure for map quality is sought. Further
 526 work is required to decide what this may be and is also necessary to evaluate which range
 527 limits would be the best choice for creating convection maps.

528 **4.2 Effect of PolarDARN Radars on Derived Convection Maps**

529 Adding PolarDARN to the dataset increases the coverage, so we would expect the
 530 CPCP to be better constrained and n to increase.

531 We find that adding the PolarDARN radars decreases the CPCP on average, which
 532 could indicate that the CPCP is overestimated without good polar cap coverage or that
 533 adding PolarDARN causes an underestimation. The latter has also been shown by Mori
 534 et al. (2012), who compared the velocity measurements from PolarDARN radars to CADI
 535 ionosonde measurements, as well as comparing the CPCP. Adding range limits to our
 536 processing will remove any slow-moving E-Region scatter, which may increase the CPCP.
 537 Without polar cap measurements, it is more likely that the CPCP is estimated inaccu-
 538 rately, which is illustrated by the example maps in Fig. S1 (c and d).

539 We also find that the difference between the HMB and Λ_{min} either stays the same
 540 or tends to increase when the polar radars are added to the dataset. Whilst we would
 541 expect PolarDARN measurements mostly to be poleward of the observations from the
 542 original high-latitude radars (particularly after introducing range limits), this does not
 543 seem to be the case, which is most likely due to the limited local time observations in
 544 the original (D0) maps. We also find that the HMB tends to stay the same or move pole-
 545 ward when adding the polar radars. This indicates that for a number of maps, the HMB
 546 was not well defined as we would not expect the introduction of PolarDARN data to move
 547 the HMB at all. Whilst this indicates that the HMB was not always necessarily well con-

548 strained prior to the introduction of the PolarDARN data, it also indicates that obser-
 549 vations near the pole are important when producing the maps.

550 Adding the PolarDARN radars to the dataset can increase or decrease χ^2/n . This
 551 parameter only tends to increase for D2 if it was low for D1 and tends to decrease for
 552 D2 if it is also high for D1. This suggests that the maps where the fitting is not partic-
 553 ularly good for D1, improve when adding PolarDARN data, but there are also a num-
 554 ber of maps where this fitting parameter decreases. Overall however, we find that the
 555 difference between the HMB and Λ_{min} has a tendency to increase, which means the HMB
 556 is constrained by data at a lower latitude. The median n increases from 40 to 108 when
 557 adding the PolarDARN radars, which is a considerable increase in scatter.

558 **4.3 Effect of StormDARN on Derived Convection Maps**

559 Adding StormDARN radars improves the coverage of data at lower latitudes, we
 560 expect the HMB to move equatorward and the CPCP to be better estimated.

561 We find that the StormDARN radars add less data to the maps (on average), than
 562 the polar or high latitude radars, but nevertheless, adding their data to the maps gen-
 563 erally improves the map quality. χ^2/n almost always decreases and the HMB tends to
 564 be better estimated. Adding StormDARN data tends to add low velocity scatter in lower
 565 turbulence regions, which better constrains the spherical harmonic expansion and lead-
 566 ing to the decrease in χ^2/n .

567 Thomas and Shepherd (2018) made a new background model and showed that in-
 568 troducing the StormDARN radars could increase the CPCP by as much as 40% (for the
 569 most strongly southward IMF conditions) due to the high-latitude radars only being able
 570 to image a proportion of the convection zone necessary to estimate the CPCP. It is worth
 571 noting that Thomas and Shepherd (2018) found very little difference in the CPCP for
 572 weak to moderate solar wind driving because the low-latitude convection boundary re-
 573 mained within the FOV of the high-latitude radars. We find that, without using the TS18
 574 model, but by simply including the StormDARN radars, the CPCP does indeed increase
 575 more often (12% of times) than decrease (8% of times) but the maximum difference seen
 576 is a 45% decrease when the CPCP varies from 34.70 kV in D2 to 19.19 kV in D3.

577 By investigating the D3 velocity measured at the HMB location of D2, we find that
 578 for 33% of cases the velocity variation is less than 200 m/s, but for a considerable num-
 579 ber of maps (8%, which equates to over 22000 maps), the velocity variation is > 400 m/s
 580 at midnight, which indicates a considerable variation to the convection pattern. This means
 581 that without the StormDARN radars, the velocities at Λ_{HMB2} could have an uncertainty
 582 of more than 190 m/s over half the time at midnight, which is considerable, assuming
 583 the HMB placement is constrained by data.

584 However, we have to consider the possibility that the HMB placing is not always
 585 as good as we would like: Many convection maps from the post-StormDARN era (such
 586 as the map shown in Fig. S1h, for example) show large amounts of low velocity mid-latitude
 587 convection in the nightside ionosphere, which does not seem to improve the convection
 588 map. We postulate that these streams are associated with magnetic flux frozen into the
 589 plasmasphere (the inner part of the magnetosphere located just above the ionosphere)
 590 (Ribeiro et al., 2012). As the plasmasphere corotates with Earth, radars should not mea-
 591 sure Doppler velocities associated with the rotation due to their fixed geographic loca-
 592 tion. However, if this co-rotation is not perfectly in sync with Earth’s rotation then it
 593 may be possible to measure low Doppler velocities (tens-hundreds of ms^{-1}). While more
 594 transient in nature, over- or under-shielding scenarios may also lead to uncertainties in
 595 the HMB latitude determination when including the StormDARN radar data (e.g. Nishida,
 596 1968; Nishitani et al., 2019): When this happens, the electric field formed at the inner
 597 edge of the plasma sheet and associated with the region 2 field-aligned currents coun-
 598 teracts the effects of the solar wind-driven magnetospheric convection at sub-auroral lat-
 599 itudes. Whilst these scenarios may lead to uncertainty of the HMB placement, they are
 600 understood to be exceptional circumstances and not well enough understood to be ex-
 601 plicitly taken into account when determining the HMB (Nishitani et al., 2019). Further-
 602 more, it is important to keep in mind that the HMB is a boundary condition, introduced
 603 to facilitate the fitting process and may in reality be different to our simplified circular
 604 shape.

605 **4.4 Effect of Changing the Background Model on Derived Convection** 606 **Maps**

607 When changing the background model from RG96 to TS18 we might expect a more
 608 realistic fit due to a background model parametrization with more variables. The TS18

609 model not only uses the IMF magnetic field strength and direction, but this model parametriza-
 610 tion also includes the solar wind's electric field and the Earth's dipole tilt, which results
 611 in 120 model bins that are trilinearly interpolated between to achieve smoother transi-
 612 tions, as opposed to the rigid 24 model bins chosen by RG96. The χ^2/n distribution in-
 613 dicates that sometimes this expected improvement is the case, however sometimes the
 614 fitting is worse (i.e. χ^2/n increases), which is primarily the case for low n maps. Over-
 615 all, we find (in Fig. 3 and 5) that the largest differences in the CPCP are produced when
 616 the CPCP was already high in D3 and these tend to occur when n is low. In fact, a higher
 617 n , means smaller likelihood of observing a difference in CPCP. Thomas and Shepherd
 618 (2018) compared the statistical averages over a ~ 7 year period and found that the CPCP
 619 can differ by as much as 40%, when StormDARN radars are included in the convection
 620 model, which is equivalent to a difference of 32 kV for a CPCP of 80 kV without the Stor-
 621 mDARN radars. In comparison, this study compares individual 2-min maps over a sim-
 622 ilar ~ 7 year period and shows that when using this model, the maximum observed per-
 623 centage difference in the CPCP is however a much larger difference: a reduction of 63%
 624 for a CPCP across this study of 49 kV in D3, which reduces to 18 kV in D4. The largest
 625 increases we find in CPCP when going from D3 to D4 is 57 kV, which happens for a CPCP
 626 of 33 kV in D3 and is a smaller difference than the smallest decrease (44 kV), which hap-
 627 pens for a CPCP of 78 kV in D3.

628 Fig. 5 and 6 show that both AL and Sym-H show a linear trend in the likelihood
 629 of observations with HMB: As the HMB tends to lower latitudes, the values in AL and
 630 Sym-H tend to be enhanced until the HMB reaches a latitude of $\sim 50^\circ$, at which point
 631 the observational likelihood reduces drastically overall. We also find that at HMBs $< 50^\circ$,
 632 n is likely to be smaller in general also, which means the observations in this HMB range
 633 are less dense and less well constrained. This is not surprising, as not all radars are ca-
 634 pable of measuring HMBs $< 50^\circ$. Furthermore, the coverage from radars at mid-latitudes
 635 is sparser as the radars tend to, on average, return less backscatter per radar than the
 636 higher latitude radars.

637 We also explored how adding the newest radars to the dataset, affects the convec-
 638 tion maps (D0 to D4 comaprison). This shows that the HMB is more likely to be found
 639 at lower latitudes ($50-40^\circ$) for D4 due to the lower observational latitude limit of the data.
 640 This means that the HMB is more likely to be observed at lower latitudes when the au-
 641 roral electrojet indices (AL and AE) are enhanced. It is possible that the observational

642 peak in AL and HMB, which shifts from ~ 400 nT in D0 to ~ 300 nT in D4 and $\sim 66^\circ$
 643 in D0 to $\sim 50^\circ$ in D4, respectively, is still limited by radar coverage and it is possible that
 644 the decreasing trend we see in the median should continue (see crosses in Fig. 6d and
 645 e). It is important to note however, that AL and AE are measured by 12 magnetome-
 646 ter stations and the current system which they measure may well move equatorward dur-
 647 ing times of high activity. This will mean that the values shown are an underestimate
 648 rather than a true estimate.

649 The RG96 model was built only using the data from the Goose Bay radar, which
 650 is located at a high-latitude and thus part of our D0 set. Whilst it is one of the oldest
 651 operating radars in the network (and thus a lot of data is available), the RG96 model
 652 was constrained in magnetic latitudes from $65\text{--}85^\circ$ (Ruohoniemi & Greenwald, 1996). It
 653 is therefore interesting to find χ^2/n reduced, when adding the StormDARN radars. This
 654 shows that the data is important in generating the convection map files, but from com-
 655 paring D3 and D4 we show that the model can also make a difference. It is however worth
 656 noting that due to its limited data ingestion, the RG96 model was not built to be used
 657 with a radar network that extends to mid-latitudes, whereas TS18 was. Regardless of
 658 the χ^2/n statistic not always decreasing for the variation from D3 to D4, the RG96 model
 659 does not account for as wide a variety of solar wind driving, dipolar tilt and latitudinal
 660 changes of the pattern and it thus makes more sense to use the TS18 model for the ex-
 661 tended dataset, especially when including data from the midlatitudes.

662 **4.5 The Importance of Parametrizing the HMB**

663 Much more than just flow velocities are affected by the HMB placement. The lo-
 664 cation of the HMB determines the boundary of the fitting, but if the CPCP is kept the
 665 same, the convection strength estimate will differ. Similarly, if the flows are kept the same,
 666 the CPCP will differ. Having a reliable HMB is therefore paramount to having a reli-
 667 able map. We have seen variations of the HMB location of up to 35° (e.g. Fig. 1) when
 668 StormDARN radar data are included. This shows that there is a great uncertainty in
 669 the placement of the HMB and good spatial coverage is paramount to ascertain the re-
 670 liability of this.

671 In either case, the HMB may need to be redefined. Currently, the HMB is calcu-
 672 lated to be where velocity measurements suggest the electric field is zero, however low

673 velocity measurements associated with imperfect co-rotation will also have an associated
674 non-zero electric field. This suggests the HMB would not give the boundary of the con-
675 vective regions associated with opening and closing of magnetic flux or that the bound-
676 ary presents as a gradual variation.

677 A further alternative to the HMB fitting could be the original fitting by Heppner
678 and Maynard (1987), who used spacecraft passes to determine the HMB location. This
679 parameterization not only provides a non-circular fit, but also one parametrized by Kp,
680 so it could be used as an alternative for the HMB fitting. The planetary K-index, Kp,
681 is a measure of global geomagnetic activity (e.g. Matzka et al., 2021, and references therein).
682 Whilst this is one of the most extensively used indices, it is a 3 hourly index, which is
683 a long timescale in the context of ionospheric convection. There is a reason why we do
684 not produce convection maps at a 3-hourly cadence: ionospheric convection can and usu-
685 ally does differ on much shorter timescales. For example, Walach and Grocott (2019) and
686 Walach et al. (2021) showed that during very active times, such as geomagnetic storms,
687 ionospheric convection and in particular the location of the HMB, varies on timescales
688 of minutes and we thus do not advise to use a Kp parameterized HMB model. Walach
689 and Grocott (2019) showed that during geomagnetic storms, which can also be described
690 as extremely driven times, the HMB can move to latitudes as low as 40° , which Super-
691 DARN radars prior to the mid-latitude expansion were not able to observe.

692 Fogg et al. (2020) provide an alternative fit for the HMB using AMPERE data, and
693 show that the HMB may be placed at too low latitudes when StormDARN data are avail-
694 able. This might indicate that a changing HMB is not always an improvement when it
695 moves equatorward in D3. It is however worth noting that the fitting by Fogg et al. (2020)
696 does not include mid-latitude data and their fitting stops at 55° , so further analysis is
697 necessary, which will be the subject of a future study.

698 Sub-auroral Polarization Streams (SAPS) are one of the main phenomenon stud-
699 ied with the StormDARN radars (e.g. Kunduri et al., 2017, 2018), which may also af-
700 fect HMB parametrization. They consist of fast azimuthal streams, measured below au-
701 roral latitudes on the nightside (Kunduri et al., 2018). The possibility of the midlatitude
702 radars observing either auroral flows in an expanded pattern, or sub-auroral flows in a
703 smaller sized pattern, is an important distinction, which we have not studied in this pa-
704 per but warrants further investigation. Kunduri et al. (2018) studied these flows in great

705 detail and found that their occurrence and flow speed tends to increase with higher ge-
 706 omagnetic activity. To this date, SAPS have not been explicitly taken into account in
 707 the background SuperDARN models (e.g. RG96 and TS18) and it is thus likely that their
 708 effects are averaged over. We know that SAPS will occur at or near the lower latitudi-
 709 nal boundary of the convection patterns (e.g. Kunduri et al., 2018), but further inves-
 710 tigation is necessary to understand how they fit in with the general convection pattern
 711 and in particular, how they affect HMB determination.

712 **4.6 The Importance of Backscatter Echoes**

713 Historically, n has on average increased due to the expansion of SuperDARN. Nev-
 714 ertheless, when we compare our most historic version of the dataset (D0) with the ver-
 715 sion that includes all new radars, as well as updated processing techniques (TS18 and
 716 range limits), we show that sometimes n decreases (Fig. 2a). This is thus solely due to
 717 introducing range limits. Whilst adding the newer radars to the dataset can in some cases
 718 increase n by 500 or more, adding range limits can reduce n by 100. We have shown that
 719 n is an important parameter in constraining the convection pattern (e.g. HMB or CPCP):
 720 In particular, we find that if n is high, the CPCP is less likely to differ (i.e. the maps are
 721 constrained well) and the HMB is more likely to be found at lower latitudes (see Fig. 5).

722 When using SuperDARN maps, the reliability of the map is important and often
 723 this has been tied to n . If n is high, the maps are often deemed more reliable (e.g. Imber
 724 et al. (2013) identified 200 to be a low threshold number for good convection maps but
 725 Fogg et al. (2020) chose 400 as threshold for an acceptable number of grid cells contain-
 726 ing data and Lockwood and McWilliams (2021) used a threshold of 255 for specifying
 727 the transpolar voltage). This raises the question of whether there is a universal thresh-
 728 old for n , which can be used to select reliable convection maps?

729 In Fig. 7b and c we show that when n is large, χ^2/n is unlikely to differ between
 730 the two datasets (the χ^2/n ratio tends to unity). However, in Fig. 7a we also show that
 731 this ratio is closest to unity when the difference in n between the two datasets is large
 732 (>200). This means that large differences in n between the datasets can have little im-
 733 pact on χ^2/n .

734 We see that for smaller n (< 200), the map fitting is more sensitive to differences
 735 between the datasets (χ^2/n varies by a factor of up to 40). In Fig 7a we see that when

736 n is the same in both datasets the χ^2/n ratio can be large or small (either D0 or D4 be-
 737 ing better constrained). In general, χ^2/n is likely to be larger in D4 than in D0 (the dis-
 738 tributions of χ^2/n ratio are skewed towards positive values in Fig. 7b and c).

739 Overall, whilst the biggest differences in χ^2/n are found only for $n < 200$, there
 740 is no clear threshold of n above which χ^2/n becomes completely insensitive to differences
 741 between the datasets, but we show that if we choose $n > 400$, χ^2/n is unlikely to differ
 742 by much and thus the map fitting is less sensitive to changes in the dataset.

743 Fig. 7b and c shows that the spread of observations becomes larger for small n and
 744 the χ^2/n ratio approaches 1 for higher n . This means that for high n , χ^2/n is likely to
 745 remain the same, so for small n , the maps are more likely to change when comparing D0
 746 and D4. This could be due to a number of reasons, but we suggest one main cause: D4
 747 includes data over a larger spatial range but for a sixth order SHA, only 49 vectors are
 748 required to constrain the fitting. This is to say that a sixth order SHA can be fully de-
 749 scribed by 49 vectors if they are spaced appropriately. As more vectors are added (e.g.
 750 from the midlatitude radars), it is likely that they are adding detail that the sixth or-
 751 der cannot resolve and thus χ^2/n is not changing drastically.

752 This study has not considered the spatial distribution of n in detail, which is likely
 753 to further influence map quality. Coverage at a range of local times and latitudes is likely
 754 to better constrain the map fitting procedure and this is something which needs to be
 755 explored further. SuperDARN map quality is inherently difficult to assess without an
 756 independent dataset and the definition of quality can be different, depending on the type
 757 of scientific study (e.g. for a case study, spatial distribution may be a crucial measure
 758 of quality). Another way to understand quality is to consider quantitative error estimates.
 759 The SuperDARN assimilative mapping technique from Cousins et al. (2013) for exam-
 760 ple, readily provides uncertainty estimates on the potential at all spatial points.

761 **4.7 Geomagnetic Conditions and SuperDARN Observations**

762 We have shown in Fig. 5 and 6 that when AL and Sym-H are enhanced, and the
 763 HMB is at lower latitudes, n tends to also be high. It is worth considering the under-
 764 lying physics and how these parameters are related.

765 The expanding and contracting polar cap paradigm (e.g. Siscoe & Huang, 1985;
 766 Lockwood, 1991; Lockwood & Cowley, 1992; Milan, 2015; Walach et al., 2017, and ref-
 767 erences therein) requires the polar cap to increase in size when the dayside reconnection
 768 rate exceeds the nightside reconnection rate. This implies that the CPCP also increases
 769 when dayside driving is high. We have shown that this is mostly the case, although there
 770 are some deviations to this relationship, which we attribute to noise and errors in solar
 771 wind propagation. It has long been discussed whether or not the relationship between
 772 the dayside driving and the CPCP is linear and whether or not the CPCP saturates be-
 773 yond a threshold (e.g. Hill et al., 1976; Reiff et al., 1981; Doyle & Burke, 1983; Wygant
 774 et al., 1983; Shepherd, 2007; Mori & Koustov, 2013, and references therein). Shepherd
 775 et al. (2002) and Shepherd (2007) discuss this in great detail and showed, using Super-
 776 DARN CPCP measurements, that during high solar wind driving (when the reconnect-
 777 ion electric field is above 5.5 mV/m), the CPCP saturates.

778 Mori and Koustov (2013) talk about a SuperDARN “quantization” effect, whereby
 779 for high CPCP where the observational density is low and not all maps are well constrained.
 780 In this case, the CPCP oftentimes takes on the values of the underlying model, which
 781 are quantized bins for RG96. We see this quantization very clearly in Figs. 3a, 3b, 3c
 782 and to some extent in Figs. 3d and 6f for RG96, but the quantization problem is solved
 783 for TS18, which interpolates between solutions of the background model. Whilst this is
 784 not the focal point of our study, we find that as Φ_D increases, the CPCP also increases.
 785 Similar to Shepherd (2007), we note that observational density is an important factor
 786 when considering the behaviour of these parameters. We also find that depending on the
 787 dataset used (e.g. D0 or D4), the trend and steepness of the curve varies due to obser-
 788 vational density of high CPCP for D0 being much lower than for D4. Furthermore, we
 789 find that the spread in values is much higher than observed by Shepherd (2007), which
 790 is due to a larger sample size (they only used equinox data for their study) and shorter
 791 sampling (they used 10 minute cadence for their map files whereas we use 2 minutes).
 792 We suggest that using the verb “saturate” to describe the behaviour of these param-
 793 eters is misplaced, as even at high values of Φ_D the CPCP increases, whereas a satura-
 794 tion implies the gradient of the curve reaching 0.

795 Whilst n is high when AL, Sym-H and the HMB are enhanced, we are not suggest-
 796 ing that the correlation equates to a causal link. This was already discussed by Walach
 797 and Grocott (2019), who showed that the number of backscatter echoes tends to increase

798 during geomagnetic storms (when Sym-H is enhanced), as dayside driving increases, the
 799 polar cap grows and the HMB moves to lower latitudes. Currie et al. (2016) showed how-
 800 ever that during intense geomagnetic storms, a reduction of backscatter was observed
 801 in the Bruny Island radar in the middle- to far-ranges, and an increase in the amount
 802 of backscatter from close-ranges. Here we show statistically, that as Sym-H is enhanced,
 803 the HMB moves to lower latitudes and the number of backscatter echoes increases for
 804 mid-ranges (the far- and close- ranges were removed beyond D0 by range limits). We thus
 805 find that the relationships found by Walach and Grocott (2019) hold statistically, though
 806 a large amount of variation is observed.

807 Wild and Grocott (2008) conducted a study (before the availability of StormDARN
 808 radars) of regions where backscatter is lost during isolated substorms, and the progres-
 809 sion through the phases of the substorm due to auroral absorption. They identify that
 810 backscatter reduction is greatest at $\sim 70\text{-}80^\circ$ magnetic latitude region between ~ 19 to
 811 03 MLT. However, Wild and Grocott (2008) also observe that the main backscatter re-
 812 gion shifts equatorward to lower latitudes (below $\sim 65^\circ$) across all local times. Our re-
 813 sults support this statistically, as we find that the StormDARN radars do on average ob-
 814 serve more backscatter, and that the backscatter moves to lower latitudes when AL is
 815 enhanced (which is expected to be the case for substorms). We also find that this trend
 816 differs slightly for D0 and D4: due to better coverage with the StormDARN radars, the
 817 HMB for D4 moves to lower latitudes than for D0. The trend of decreasing HMB with
 818 decreasing AL is a statistical one and thus breaks at a latitudes close to $\sim 40^\circ$ due to low
 819 observational densities

820 **4.8 Is χ^2/n an Adequate Measure of Map Quality?**

821 The current most simple way to assess map quality is to look at the χ^2/n statis-
 822 tic. In this study we have explored χ^2/n as a way to measure the quality of the fitting
 823 to the line-of-sight data as defined in the Data and Methods section of this paper. If we
 824 sum χ^2 and divide by the sum of n for each dataset D0 to D4, we obtain the following
 825 average values: $\langle \chi^2/n \rangle_{D0}$: 1.70; $\langle \chi^2/n \rangle_{D1}$: 2.01; $\langle \chi^2/n \rangle_{D2}$: 2.16; $\langle \chi^2/n \rangle_{D3}$:
 826 1.88; and $\langle \chi^2/n \rangle_{D4}$: 1.81.

827 From this, we might conclude that D0 has overall the highest quality maps and is
 828 closest to the “good match” criterion (1) identified by Ruohoniemi and Baker (1998),

829 but we have shown that whilst the map fitting may be better for D0, the missing data
 830 also equates to a qualitative penalty. A map could have a χ^2/n close to 1 (i.e. a “good”
 831 fit), but only have 10 closely clustered vectors, in which case the map is unreliable. We
 832 find from the χ^2/n distributions that most of the impact on χ^2/n are provided by range
 833 limits and the addition of the StormDARN radar data. This emphasizes the importance
 834 of good spatial coverage. We also see from these statistics, that overall, the TS18 model
 835 improves map fitting.

836 Furthermore, at high latitudes, in the auroral zone and polar cap, fluctuations in
 837 the velocity can be greater due to increased turbulence. These velocities are more likely
 838 to fit badly with low order spherical harmonic fits (~ 6) leading to larger increases in χ^2/n .
 839 Hence, the removal of far-range scatter will obviously reduce the average χ^2/n . Conversely,
 840 low velocity scatter measured in regions of lower turbulence at low latitudes fits better
 841 to the spherical harmonic expansion and will have a smaller contribution to χ^2 per scat-
 842 ter point (regardless of order), and so the addition of more low-latitude low-velocity data
 843 will again reduce the average χ^2/n . Consequently, an amount of low latitude scatter will
 844 have a much smaller contribution to χ^2/n than the same amount of higher latitude scat-
 845 ter. But an increased goodness of fit does not always mean a “better” map. There are
 846 many example maps (such as those provided in Fig. S1c and d) in which a low χ^2/n does
 847 not always equate to a higher quality map. True quality is however difficult to appraise.
 848 In order to achieve this, one would have to define quality first, which is beyond the scope
 849 of this study. In order to truly establish map quality, we recommend the close inspec-
 850 tion of the individual maps and comparison with independent data, where available (e.g.
 851 Walach et al., 2017).

852 5 Summary

853 We have investigated how the SuperDARN maps have changed historically by cre-
 854 ating 5 different versions of the convection map files for a timespan of 6 years and com-
 855 paring them statistically. By using different processing parameters and gradually intro-
 856 ducing more data to the maps, we were able to investigate how the derived convection
 857 maps differ with the inclusion of

- 858 • backscatter range limits (as was used by Thomas and Shepherd (2018))
- 859 • the polar cap radars, PolarDARN

- 860 • the mid-latitude radars, StormDARN
- 861 • a different background model (we compare Thomas and Shepherd (2018) and Ruohoniemi
- 862 and Greenwald (1996))

863 We have shown that

- 864 • introducing range limits does not always decrease χ^2/n ,
- 865 • n is not a good predictor for how good the fit is once range limits have been ap-
- 866 plied
- 867 • once range limits have been applied the CPCP stays the same 30% of the time and
- 868 the HMB stays constant most of the time (54%)
- 869 • the addition of PolarDARN data tends to reduce the CPCP,
- 870 • PolarDARN radars add the most data to the dataset (on average), but the Stor-
- 871 mDARN radars are also important for constraining the maps,
- 872 • when introducing StormDARN radars to the maps, the χ^2/n values tend to de-
- 873 crease, the HMB becomes better constrained and the CPCP tends to increase
- 874 • when changing the background model to TS18, the CPCP tends to decrease for
- 875 lower values of the CPCP in RG96, but is more likely to increase for larger val-
- 876 ues of the CPCP in RG96. If n is however high (> 400), the CPCP is less likely
- 877 to differ (differences $\sim < 20$ kV).
- 878 • as n , AL and Sym-H all increase, the HMB tends to go to lower latitudes, which
- 879 appears to be a linear trend, though a break is seen at HMB ~ 50 degrees, where
- 880 the observational density drops off sharply.
- 881 • if n is high, the CPCP is less likely to differ and the HMB is more likely to be found
- 882 at lower latitudes and χ^2/n tends to differ by the least amount,
- 883 • there is no clear break, where n universally produces good convection maps, but
- 884 we show that for $n > 400$, χ^2/n is unlikely to differ by much and thus the map
- 885 is well constrained.

886 Naturally, assessing map quality has to include a qualitative discussion and we have
 887 found that there is currently no perfect quantitative method for this assessment.

888 SuperDARN provides a powerful tool for assessing solar wind-magnetosphere-ionosphere
 889 coupling and studying responses to solar wind driving of the system. Due to observa-
 890 tions being available almost all the time, and new radars having been constructed over

891 the years, the dataset now spans several decades and is well-understood. We have pre-
 892 sented a statistical analysis, which shows that the measured parameters (such as the CPCP
 893 and HMB) differ little on average, though in some circumstances they can be highly sus-
 894 ceptible to which processing parameters are used, as well as which radars are used when
 895 generating map files. We have shown that most of the time, parameters such as the CPCP
 896 are unlikely to change by a large amount. However, when SuperDARN maps are used
 897 for studies of specific conditions or small case studies, as a sampling bias can occur. As
 898 a result, care has to be taken when processing the data. We have found that a high num-
 899 ber of SuperDARN backscatter echoes are particularly important when constraining maps,
 900 so it is important to include StormDARN data in the generation of SuperDARN con-
 901 vection maps. The variety of conditions that we see in our statistical comparison illus-
 902 trates how rich the SuperDARN dataset is. Furthermore, we have illustrated concepts
 903 which can be improved. For example, we have also shown that χ^2/n is not an adequate
 904 measure of map quality and whilst the HMB is largely well-defined, the method can still
 905 be improved. Further work is thus necessary to evaluate convection map quality and gen-
 906 erate a robust HMB selection method, especially at lower latitudes.

907 **Appendix A SuperDARN processing parameters**

908 In the SuperDARN processing (see section 2), we use the following parameters and
 909 functions from RST:

- 910 • For fitting the autocorrelation function to the raw data: 'make_fit' with the op-
 911 tion '-fitacf-version 2.5'.
- 912 • To make the gridded map files, the options '-i 120 -tl 120 -chisham -c' were added
 913 to 'make_grid'
- 914 • To add the range limits to the gridded files, the same options as above were used
 915 but in addition, the options '-minsrng 800 -maxsrng 2000' were added.
- 916 • The function 'map_grd' was used with 'map_addhmb -vel 100 -cnt 3'. Adding these
 917 options to 'map_addhmb' chooses the Heppner-Maynard boundary to the lowest
 918 possible latitude for which a minimum of three LOS vectors with velocities greater
 919 than 100 m/s lie along its boundary.

- 920 • To make the convection maps, we also use 'map_addimf -if' with the text file con-
921 taining the IMF data and the option '-df' with the text file containing the IMF
922 delay times.
- 923 • We then use 'map_addmodel -o 6 ' for a sixth order expansion and use '-d' to spec-
924 ify a light doping level.
- 925 • Finally, we add the model option '-rg96' to D0-D3 and '-ts18' to D4 and use the
926 function 'map_fit' to make the convection map files.
- 927 • We also use the function 'cnvmaptomap' to convert the binary file to ASCII for-
928 mat and 'trim_map' with the options '-st', '-et', '-sd' and '-ed' to make two-hour
929 long map files for our archive, but this is not necessary to obtain the results for
930 this study.

931 **Acknowledgments**

932 All data used for this study are available opensource from nonprofit organizations. The
933 authors acknowledge the use of SuperDARN data. SuperDARN is a collection of radars
934 funded by national scientific funding agencies of Australia, Canada, China, France, Italy,
935 Japan, Norway, South Africa, United Kingdom, and United States of America, and we
936 thank the international PI team for providing the data. The authors acknowledge ac-
937 cess to the SuperDARN database via the British Antarctic Survey (<https://www.bas.ac.uk/project/superdarn/#d>)
938 Other data mirrors are hosted by the Virginia Tech SuperDARN group (<http://vt.superdarn.org/>)
939 and the University of Saskatchewan (<https://superdarn.ca/data-download>). The Radar
940 Software Toolkit (RST) to process the SuperDARN data can be downloaded from Zen-
941 odo (<https://doi.org/10.5281/zenodo.1403226> and references). All solar wind data and
942 geomagnetic indices were downloaded from NASA's SPDF Coordinated Data Analysis
943 Web (<https://cdaweb.gsfc.nasa.gov/index.html/>). The AE data is also available from the
944 WDC for Geomagnetism, Kyoto (<http://wdc.kugi.kyoto-u.ac.jp/wdc/Sec3.html>) who pre-
945 pared this index. M.-T. W. and A. G. were supported by Natural Environments Research
946 Council (NERC), UK, grant nos. NE/P001556/1 and NE/T000937/1. F. S. was supported
947 by a Science and Technology Funding Council (STFC) studentship. E. G. T. thanks the
948 National Science Foundation (NSF) for support under grants AGS-1934997 and OPP-
949 1836426. We gratefully acknowledge the use of Lancaster University's High End Com-
950 puting Cluster, which has facilitated the necessary dataprocessing for this study. M.-T.
951 W. would like to thank LU's Women's Network Writing Group for providing a support-

952 ive virtual writing space and mentorship, which helped to forge this paper. M.-T. W.
953 also thanks Gareth Chisham and Mark Lester for the discussions, which helped improve
954 this paper.

955 References

- 956 Chisham, G., Lester, M., Milan, S. E., Freeman, M. P., Bristow, W. A., Grocott, A.,
957 ... Walker, D. M. (2007). A decade of the Super Dual Auroral Radar Network
958 (SuperDARN): Scientific achievements, new techniques and future directions.
959 *Surveys in Geophysics*, *28*(1), 33–109. doi: 10.1007/s10712-007-9017-8
- 960 Chisham, G., & Pinnock, M. (2002). Assessing the contamination of SuperDARN
961 global convection maps by non-F-region backscatter. *Annales Geophysi-*
962 *caae*, *20*(1), 13-28. Retrieved from [https://hal.archives-ouvertes.fr/](https://hal.archives-ouvertes.fr/hal-00316917)
963 [hal-00316917](https://hal.archives-ouvertes.fr/hal-00316917)
- 964 Chisham, G., Yeoman, T. K., & Sofko, G. J. (2008). Mapping ionospheric
965 backscatter measured by the superdarn hf radars – part 1: A new empir-
966 ical virtual height model. *Annales Geophysicae*, *26*(4), 823–841. doi:
967 10.5194/angeo-26-823-2008
- 968 Cousins, E. D. P., Matsuo, T., & Richmond, A. D. (2013). Superdarn assimila-
969 tive mapping. *Journal of Geophysical Research: Space Physics*, *118*(12), 7954-
970 7962. Retrieved from [https://agupubs.onlinelibrary.wiley.com/doi/abs/](https://agupubs.onlinelibrary.wiley.com/doi/abs/10.1002/2013JA019321)
971 [10.1002/2013JA019321](https://agupubs.onlinelibrary.wiley.com/doi/abs/10.1002/2013JA019321) doi: 10.1002/2013JA019321
- 972 Cousins, E. D. P., & Shepherd, S. G. (2010). A dynamical model of high-latitude
973 convection derived from superdarn plasma drift measurements. *Journal of Geo-*
974 *physical Research: Space Physics*, *115*(A12). Retrieved from [https://agupubs](https://agupubs.onlinelibrary.wiley.com/doi/abs/10.1029/2010JA016017)
975 [.onlinelibrary.wiley.com/doi/abs/10.1029/2010JA016017](https://agupubs.onlinelibrary.wiley.com/doi/abs/10.1029/2010JA016017) doi: 10.1029/
976 2010JA016017
- 977 Currie, J. L., Waters, C. L., Menk, F. W., Sciffer, M. D., & Bristow, W. A. (2016).
978 Superdarn backscatter during intense geomagnetic storms. *Radio Science*,
979 *51*(6), 814-825. Retrieved from [https://agupubs.onlinelibrary.wiley](https://agupubs.onlinelibrary.wiley.com/doi/abs/10.1002/2016RS005960)
980 [.com/doi/abs/10.1002/2016RS005960](https://agupubs.onlinelibrary.wiley.com/doi/abs/10.1002/2016RS005960) doi: 10.1002/2016RS005960
- 981 Davis, T. N., & Sugiura, M. (1966). Auroral electrojet activity index ae and its
982 universal time variations. *Journal of Geophysical Research (1896-1977)*, *71*(3),
983 785-801. Retrieved from <https://agupubs.onlinelibrary.wiley.com/>

- 984 doi/abs/10.1029/JZ071i003p00785 doi: <https://doi.org/10.1029/>
985 JZ071i003p00785
- 986 Doyle, M. A., & Burke, W. J. (1983). S3-2 measurements of the polar cap po-
987 tential. *Journal of Geophysical Research*, 88(A11), 9125. doi: 10.1029/
988 JA088iA11p09125
- 989 Fogg, A. R., Lester, M., Yeoman, T. K., Burrell, A. G., Imber, S. M., Milan,
990 S. E., ... Anderson, B. J. (2020). An improved estimation of superdarn
991 heppner-maynard boundaries using ampere data. *Journal of Geophysical Re-*
992 *search: Space Physics*, 125(5), e2019JA027218. Retrieved from [https://](https://agupubs.onlinelibrary.wiley.com/doi/abs/10.1029/2019JA027218)
993 agupubs.onlinelibrary.wiley.com/doi/abs/10.1029/2019JA027218
994 (e2019JA027218 10.1029/2019JA027218) doi: <https://doi.org/10.1029/>
995 2019JA027218
- 996 Forsythe, V. V., & Makarevich, R. A. (2017). Global view of the e region irreg-
997 ularity and convection velocities in the high-latitude southern hemisphere.
998 *Journal of Geophysical Research: Space Physics*, 122(2), 2467-2483. Retrieved
999 from [https://agupubs.onlinelibrary.wiley.com/doi/abs/10.1002/](https://agupubs.onlinelibrary.wiley.com/doi/abs/10.1002/2016JA023711)
1000 2016JA023711 doi: <https://doi.org/10.1002/2016JA023711>
- 1001 Greenwald, R. A., Baker, K. B., Dudeney, J. R., Pinnock, M., Jones, T. B., Thomas,
1002 E. C., ... Yamagishi, H. (1995). Darn/superdarn. *Space Science Reviews*,
1003 71(1), 761-796. doi: 10.1007/BF00751350
- 1004 Heppner, J. P., & Maynard, N. C. (1987). Empirical high-latitude electric field
1005 models. *Journal of Geophysical Research*, 92(A5), 4467-4489. doi: 10.1029/
1006 JA092iA05p04467
- 1007 Hill, T. W., Dessler, A. J., & Wolf, R. A. (1976). Mercury and mars: The role
1008 of ionospheric conductivity in the acceleration of magnetospheric particles.
1009 *Geophysical Research Letters*, 3(8), 429-432. Retrieved from [https://](https://agupubs.onlinelibrary.wiley.com/doi/abs/10.1029/GL003i008p00429)
1010 agupubs.onlinelibrary.wiley.com/doi/abs/10.1029/GL003i008p00429
1011 doi: <https://doi.org/10.1029/GL003i008p00429>
- 1012 Imber, S. M., Milan, S. E., & Lester, M. (2013). The heppner-maynard bound-
1013 ary measured by superdarn as a proxy for the latitude of the auroral oval.
1014 *Journal of Geophysical Research: Space Physics*, 118(2), 685-697. doi:
1015 10.1029/2012JA018222
- 1016 Iyemori, T. (1990). Storm-time magnetospheric currents inferred from mid-latitude

- 1017 geomagnetic field variations. *Journal of geomagnetism and geoelectricity*,
 1018 *42*(11), 1249-1265. doi: 10.5636/jgg.42.1249
- 1019 Khan, H., & Cowley, S. W. H. (1999, Sep 01). Observations of the response time
 1020 of high-latitude ionospheric convection to variations in the interplanetary
 1021 magnetic field using eiscat and imp-8 data. *Annales Geophysicae*, *17*(10),
 1022 1306–1335. doi: 10.1007/s00585-999-1306-8
- 1023 Kunduri, B. S. R., Baker, J. B. H., Ruohoniemi, J. M., Nishitani, N., Ok-
 1024 savik, K., Erickson, P. J., ... Miller, E. S. (2018). A new empirical
 1025 model of the subauroral polarization stream. *Journal of Geophysical Re-*
 1026 *search: Space Physics*, *123*(9), 7342-7357. Retrieved from [https://](https://agupubs.onlinelibrary.wiley.com/doi/abs/10.1029/2018JA025690)
 1027 agupubs.onlinelibrary.wiley.com/doi/abs/10.1029/2018JA025690 doi:
 1028 <https://doi.org/10.1029/2018JA025690>
- 1029 Kunduri, B. S. R., Baker, J. B. H., Ruohoniemi, J. M., Thomas, E. G., Shepherd,
 1030 S. G., & Sterne, K. T. (2017, June). Statistical characterization of the large-
 1031 scale structure of the subauroral polarization stream. *J. Geophys. Res-Space*
 1032 *Phys.*, *122*(6), 6035–6048. doi: 10.1002/2017JA024131
- 1033 Lockwood, M. (1991). On flow reversal boundaries and transpolar voltage in average
 1034 models of high-latitude convection. *Planetary and Space Science*, *39*(3), 397–
 1035 409. doi: 10.1016/0032-0633(91)90002-r
- 1036 Lockwood, M., & Cowley, S. W. H. (1992). Ionospheric convection and the substorm
 1037 cycle. In *International conference on substorms*.
- 1038 Lockwood, M., & McWilliams, K. A. (2021). A survey of 25 years' transpolar volt-
 1039 age data from the superdarn radar network and the expanding-contracting
 1040 polar cap model. *Journal of Geophysical Research: Space Physics*, *126*(9),
 1041 e2021JA029554. Retrieved from [https://agupubs.onlinelibrary.wiley](https://agupubs.onlinelibrary.wiley.com/doi/abs/10.1029/2021JA029554)
 1042 [.com/doi/abs/10.1029/2021JA029554](https://agupubs.onlinelibrary.wiley.com/doi/abs/10.1029/2021JA029554) (e2021JA029554 2021JA029554) doi:
 1043 <https://doi.org/10.1029/2021JA029554>
- 1044 Matzka, J., Stolle, C., Yamazaki, Y., Bronkalla, O., & Morschhauser, A. (2021).
 1045 The geomagnetic kp index and derived indices of geomagnetic activ-
 1046 ity. *Space Weather*, *19*(5), e2020SW002641. Retrieved from [https://](https://agupubs.onlinelibrary.wiley.com/doi/abs/10.1029/2020SW002641)
 1047 agupubs.onlinelibrary.wiley.com/doi/abs/10.1029/2020SW002641 doi:
 1048 <https://doi.org/10.1029/2020SW002641>
- 1049 Milan, S. E. (2015). Magnetospheric Plasma Physics: The Impact of Jim Dungey's

- 1050 Research. In D. Southwood, S. W. H. Cowley FRS, & S. Mitton (Eds.), *Mag-*
 1051 *netospheric plasma physics: The impact of jim dungey's research* (pp. 1–271).
 1052 doi: 10.1007/978-3-319-18359-6_2
- 1053 Milan, S. E., Gosling, J. S., & Hubert, B. (2012, mar). Relationship between inter-
 1054 planetary parameters and the magnetopause reconnection rate quantified from
 1055 observations of the expanding polar cap. *Journal of Geophysical Research*,
 1056 *117*(A3), A03226. doi: 10.1029/2011JA017082
- 1057 Mori, D., & Koustov, A. (2013). Superdarn cross polar cap potential depen-
 1058 dence on the solar wind conditions and comparisons with models. *Ad-*
 1059 *vances in Space Research*, *52*(6), 1155-1167. Retrieved from [https://](https://www.sciencedirect.com/science/article/pii/S0273117713003803)
 1060 www.sciencedirect.com/science/article/pii/S0273117713003803 doi:
 1061 <https://doi.org/10.1016/j.asr.2013.06.019>
- 1062 Mori, D., Koustov, A. V., Jayachandran, P. T., & Nishitani, N. (2012). Res-
 1063 olute bay cad i ionosonde drifts, polardarn hf velocities, and cross po-
 1064 lar cap potential. *Radio Science*, *47*(3). Retrieved from [https://](https://agupubs.onlinelibrary.wiley.com/doi/abs/10.1029/2011RS004947)
 1065 agupubs.onlinelibrary.wiley.com/doi/abs/10.1029/2011RS004947 doi:
 1066 <https://doi.org/10.1029/2011RS004947>
- 1067 Nishida, A. (1968). Coherence of geomagnetic dp 2 fluctuations with interplanetary
 1068 magnetic variations. *Journal of Geophysical Research (1896-1977)*, *73*(17),
 1069 5549-5559. Retrieved from [https://agupubs.onlinelibrary.wiley.com/](https://agupubs.onlinelibrary.wiley.com/doi/abs/10.1029/JA073i017p05549)
 1070 [doi/abs/10.1029/JA073i017p05549](https://agupubs.onlinelibrary.wiley.com/doi/abs/10.1029/JA073i017p05549) doi: [https://doi.org/10.1029/](https://doi.org/10.1029/JA073i017p05549)
 1071 [JA073i017p05549](https://doi.org/10.1029/JA073i017p05549)
- 1072 Nishitani, N., Ruohoniemi, J. M., Lester, M., Baker, J. B. H., Koustov, A. V., Shep-
 1073 herd, S. G., ... Kikuchi, T. (2019). Review of the accomplishments of mid-
 1074 latitude super dual auroral radar network (superdarn) hf radars. *Progress in*
 1075 *Earth and Planetary Science*, *6*(1), 27. doi: 10.1186/s40645-019-0270-5
- 1076 Pettigrew, E. D., Shepherd, S. G., & Ruohoniemi, J. M. (2010). Climatologi-
 1077 cal patterns of high-latitude convection in the northern and southern hemi-
 1078 spheres: Dipole tilt dependencies and interhemispheric comparisons. *Journal*
 1079 *of Geophysical Research: Space Physics*, *115*(A7). Retrieved from [https://](https://agupubs.onlinelibrary.wiley.com/doi/abs/10.1029/2009JA014956)
 1080 agupubs.onlinelibrary.wiley.com/doi/abs/10.1029/2009JA014956 doi:
 1081 [10.1029/2009JA014956](https://doi.org/10.1029/2009JA014956)
- 1082 Press, W. H. and Teukolsky, S. A. and Vetterling W. T. and Flannery B. P. (2007).

- 1083 *Numerical recipes: The art of scientific computing.* Cambridge University
1084 Press.
- 1085 Reiff, P. H., Spiro, R. W., & Hill, T. W. (1981). Dependence of polar cap potential
1086 drop on interplanetary parameters. *Journal of Geophysical Research*, *86*(A9),
1087 7639–7648. doi: 10.1029/JA086iA09p07639
- 1088 Ribeiro, A. J., Ruohoniemi, J. M., Baker, J. B. H., Clausen, L. B. N., Green-
1089 wald, R. A., & Lester, M. (2012). A survey of plasma irregularities as
1090 seen by the midlatitude blackstone superdarn radar. *Journal of Geo-*
1091 *physical Research: Space Physics*, *117*(A2). Retrieved from [https://](https://agupubs.onlinelibrary.wiley.com/doi/abs/10.1029/2011JA017207)
1092 agupubs.onlinelibrary.wiley.com/doi/abs/10.1029/2011JA017207 doi:
1093 <https://doi.org/10.1029/2011JA017207>
- 1094 Ruohoniemi, J. M., & Baker, K. B. (1998). Large-scale imaging of high-latitude con-
1095 vection with Super Dual Auroral Radar Network HF radar observations. *Jour-*
1096 *nal of Geophysical Research*, *103*(A9), 20797. doi: 10.1029/98JA01288
- 1097 Ruohoniemi, J. M., & Greenwald, R. A. (1996). Statistical patterns of high-latitude
1098 convection obtained from Goose Bay HF radar observations. *Journal of Geo-*
1099 *physical Research*, *101*(A10), 21743. Retrieved from [http://doi.wiley.com/](http://doi.wiley.com/10.1029/96JA01584)
1100 [10.1029/96JA01584](http://doi.wiley.com/10.1029/96JA01584) doi: 10.1029/96JA01584
- 1101 Ruohoniemi, J. M., & Greenwald, R. A. (2005). Dependencies of high-latitude
1102 plasma convection: Consideration of interplanetary magnetic field, seasonal,
1103 and universal time factors in statistical patterns. *Journal of Geophysical Re-*
1104 *search: Space Physics*, *110*(A09204). doi: 10.1029/2004JA010815
- 1105 Shepherd, S. G. (2007). Polar cap potential saturation: Observations, theory, and
1106 modeling. *Journal of Atmospheric and Solar-Terrestrial Physics*, *69*(3), 234-
1107 248. Retrieved from [https://www.sciencedirect.com/science/article/](https://www.sciencedirect.com/science/article/pii/S136468260600263X)
1108 [pii/S136468260600263X](https://www.sciencedirect.com/science/article/pii/S136468260600263X) (Global Aspects of Magnetosphere-Ionosphere
1109 Coupling) doi: <https://doi.org/10.1016/j.jastp.2006.07.022>
- 1110 Shepherd, S. G. (2014). Altitude-adjusted corrected geomagnetic coordinates: Def-
1111 inition and functional approximations. *Journal of Geophysical Research: Space*
1112 *Physics*, *119*(9), 7501-7521. doi: 10.1002/2014JA020264
- 1113 Shepherd, S. G., Greenwald, R. A., & Ruohoniemi, J. M. (2002). Cross polar cap
1114 potentials measured with super dual auroral radar network during quasi-steady
1115 solar wind and interplanetary magnetic field conditions. *Journal of Geo-*

- 1116 *physical Research: Space Physics*, 107(A7), SMP 5-1-SMP 5-11. Retrieved
 1117 from [https://agupubs.onlinelibrary.wiley.com/doi/abs/10.1029/](https://agupubs.onlinelibrary.wiley.com/doi/abs/10.1029/2001JA000152)
 1118 2001JA000152 doi: <https://doi.org/10.1029/2001JA000152>
- 1119 Shepherd, S. G., & Ruohoniemi, J. M. (2000). Electrostatic potential patterns in
 1120 the high-latitude ionosphere constrained by superdarn measurements. *Journal*
 1121 *of Geophysical Research: Space Physics*, 105(A10), 23005-23014. Retrieved
 1122 from [https://agupubs.onlinelibrary.wiley.com/doi/abs/10.1029/](https://agupubs.onlinelibrary.wiley.com/doi/abs/10.1029/2000JA000171)
 1123 2000JA000171 doi: 10.1029/2000JA000171
- 1124 Siscoe, G. L., & Huang, T. S. (1985). Polar cap inflation and deflation. *Journal of*
 1125 *Geophysical Research*, 90(A1), 543–547.
- 1126 SuperDARN Data Analysis Working Group, P. m., Thomas, E. G., Ponomarenko,
 1127 P. V., Billett, D. D., Bland, E. C., Burrell, A. G., ... Walach, M.-T. (2018,
 1128 August). *Superdarn radar software toolkit (rst) 4.2*. Retrieved from
 1129 <https://doi.org/10.5281/zenodo.1403226> doi: 10.5281/zenodo.1403226
- 1130 SuperDARN Data Analysis Working Group, P. m., Thomas, E. G., Ponomarenko,
 1131 P. V., Bland, E. C., Burrell, A. G., Kotyk, K., ... Walach, M.-T. (2018,
 1132 January). *Superdarn radar software toolkit (rst) 4.1*. Retrieved from
 1133 <https://doi.org/10.5281/zenodo.1143675> doi: 10.5281/zenodo.1143675
- 1134 SuperDARN Data Analysis Working Group, P. m., Thomas, E. G., Sterne, K. T.,
 1135 Shepherd, S. G., Kotyk, K., Schmidt, M. T., ... Billett, D. D. (2019, Septem-
 1136 ber). *Superdarn radar software toolkit (rst) 4.3*. Zenodo. Retrieved from
 1137 <https://doi.org/10.5281/zenodo.3401622> doi: 10.5281/zenodo.3401622
- 1138 Thomas, E. G., & Shepherd, S. G. (2018, apr). Statistical Patterns of Ionospheric
 1139 Convection Derived From Mid-latitude, High-Latitude, and Polar Super-
 1140 DARN HF Radar Observations. *Journal of Geophysical Research: Space*
 1141 *Physics*, 123(4), 3196–3216. Retrieved from [http://doi.wiley.com/10.1002/](http://doi.wiley.com/10.1002/2018JA025280)
 1142 2018JA025280 doi: 10.1002/2018JA025280
- 1143 Walach, M.-T., & Grocott, A. (2019). Superdarn observations during geomagnetic
 1144 storms, geomagnetically active times, and enhanced solar wind driving. *Jour-*
 1145 *nal of Geophysical Research: Space Physics*, 124(7), 5828-5847. Retrieved
 1146 from [https://agupubs.onlinelibrary.wiley.com/doi/abs/10.1029/](https://agupubs.onlinelibrary.wiley.com/doi/abs/10.1029/2019JA026816)
 1147 2019JA026816 doi: 10.1029/2019JA026816
- 1148 Walach, M.-T., Grocott, A., & Milan, S. E. (2021). Average ionospheric electric field

- 1149 morphologies during geomagnetic storm phases. *Journal of Geophysical Re-*
 1150 *search: Space Physics*, 126(4), e2020JA028512. Retrieved from [https://](https://agupubs.onlinelibrary.wiley.com/doi/abs/10.1029/2020JA028512)
 1151 agupubs.onlinelibrary.wiley.com/doi/abs/10.1029/2020JA028512
 1152 (e2020JA028512 2020JA028512) doi: <https://doi.org/10.1029/2020JA028512>
- 1153 Walach, M.-T., Milan, S. E., Yeoman, T. K., Hubert, B. A., & Hairston, M. R.
 1154 (2017). Testing nowcasts of the ionospheric convection from the expand-
 1155 ing and contracting polar cap model. *Space Weather*, 15(4), 623-636. doi:
 1156 10.1002/2017SW001615
- 1157 Wild, J. A., & Grocott, A. (2008). The influence of magnetospheric substorms on
 1158 superdarn radar backscatter. *Journal of Geophysical Research: Space Physics*,
 1159 113(A4). Retrieved from [https://agupubs.onlinelibrary.wiley.com/doi/](https://agupubs.onlinelibrary.wiley.com/doi/abs/10.1029/2007JA012910)
 1160 [abs/10.1029/2007JA012910](https://agupubs.onlinelibrary.wiley.com/doi/abs/10.1029/2007JA012910) doi: 10.1029/2007JA012910
- 1161 World Data Center for Geomagnetism in Kyoto, Nose, M., Iyemori, T., Sugiura, M.,
 1162 & Kamei, T. (2015). *Geomagnetic ae index*. doi: 10.17593/15031-54800
- 1163 Wygant, J. R., Torbert, R. B., & Mozer, F. S. (1983). Comparison of s3-3 po-
 1164 lar cap potential drops with the interplanetary magnetic field and mod-
 1165 els of magnetopause reconnection. *Journal of Geophysical Research:*
 1166 *Space Physics*, 88(A7), 5727-5735. Retrieved from [https://agupubs](https://agupubs.onlinelibrary.wiley.com/doi/abs/10.1029/JA088iA07p05727)
 1167 [.onlinelibrary.wiley.com/doi/abs/10.1029/JA088iA07p05727](https://agupubs.onlinelibrary.wiley.com/doi/abs/10.1029/JA088iA07p05727) doi:
 1168 <https://doi.org/10.1029/JA088iA07p05727>